JCB Journal of Cell Biology

ARTICLE

An S-acylated N-terminus and a conserved loop regulate the activity of the ABHD17 deacylase

Sydney Holme[1,2*], Jennifer Sapia[3*], Michael Davey[2], Stefano Vanni[3,4], and Elizabeth Conibear[1,2]

The dynamic addition and removal of long-chain fatty acids modulate protein function and localization. The α/β hydrolase domain–containing (ABHD) 17 enzymes remove acyl chains from membrane-localized proteins such as the oncoprotein NRas, but how the ABHD17 proteins are regulated is unknown. Here, we used cell-based studies and molecular dynamics simulations to show that ABHD17 activity is controlled by two mobile elements—an S-acylated N-terminal helix and a loop—that flank the putative substrate-binding pocket. Multiple S-acylation events anchor the N-terminal helix in the membrane, enabling hydrophobic residues in the loop to engage with the bilayer. This stabilizes the conformation of both helix and loop, alters the conformation of the binding pocket, and optimally positions the enzyme for substrate engagement. S-acylation may be a general feature of acyl-protein thioesterases. By providing a mechanistic understanding of how the lipid modification of a lipid-removing enzyme promotes its enzymatic activity, this work contributes to our understanding of cellular S-acylation cycles.

Introduction

S-acylation, which involves the posttranslational addition of a long-chain fatty acid to cysteine residues, is the only reversible lipid modification. Dynamic S-acylation has been shown to influence protein localization, stability, and activity and is important for cellular processes such as signaling and growth (reviewed in Chen et al. [2021] and Mesquita et al. [2024]). For example, NRas undergoes a cycle of acyl chain addition and removal that regulates its localization at the plasma membrane and is essential for oncogenic signaling (Remsberg et al., 2021; Xu et al., 2012). Altered acylation dynamics are implicated in conditions ranging from cancer and inflammation to neurodegenerative and cardiovascular diseases (Lin, 2021; Main and Fuller, 2022; Ramzan et al., 2023; Zhou et al., 2023).

Two classes of enzymes regulate S-acylation cycles: the protein-acyl transferase enzymes that attach acyl chains to cytosolically exposed cysteines via a thioester bond and the acyl-protein thioesterase (APT) enzymes that remove the lipid (Greaves and Chamberlain, 2010; Won et al., 2018). While an estimated 10–20% of all human proteins are S-acylated, predominantly with the 16-carbon lipid palmitate (Muszbek et al., 1999), only a small subset of these undergoes rapid deacylation (Martin et al., 2011). Cellular APT activity can also be enhanced by growth factor signaling (Kathayat et al., 2017), suggesting APT enzymes are both substrate-selective and stimulus-responsive. However, the mechanisms that regulate their substrate binding and activity are not well understood.

The best-studied cytosolic APTs are members of the metabolic serine hydrolase family, including APT1, APT2, and the α/β hydrolase domain-containing 17 proteins ABHD17A-C (collectively referred to here as ABHD17). ABHD17 is best characterized for its activity on NRas and synaptic PSD-95 (Lin and Conibear, 2015; Yokoi et al., 2016), though the list of targets is growing (Dixon et al., 2023, *Preprint*; Remsberg et al., 2021; Ulengin-Talkish et al., 2021). Activity of ABHD17 on the stress-regulated exon variant of the large conductance voltage- and calcium-activated potassium channel, nucleotide-binding domain, leucine-rich repeat, and pyrin domain-containing protein 3, and microtubule-associated protein 6 implicates dynamic acylation in physiological processes such as cellular excitability, inflammatory disease, and neuronal maturation and development (Tortosa et al., 2017; McClafferty et al., 2020; Zheng et al., 2023). Notably, a number of other enzymes have been proposed to have thioesterase activity and are under active investigation (Cao et al., 2019; Martin et al., 2011; Rosier et al., 2021; Savinainen et al., 2014; Xu et al., 2018; Yokoi et al., 2016).

From a structural and mechanistic point of view, an interesting feature of many APTs is that they themselves are S-acylated, which directs them to membranes where their substrates are located (Kong et al., 2013; Cao et al., 2019; Martin and Cravatt, 2009). Recent work suggests that acylation of APT2 has additional regulatory functions and occurs through a multistep process involving

[1]Department of Medical Genetics, University of British Columbia, Vancouver, BC, Canada; [2]Centre for Molecular Medicine and Therapeutics, British Columbia Children's Hospital Research Institute, University of British Columbia, Vancouver, BC, Canada; [3]Department of Biology, University of Fribourg, Fribourg, Switzerland; [4]Swiss National Center for Competence in Research Bio-Inspired Materials, University of Fribourg, Fribourg, Switzerland.

*S. Holme and J. Sapia contributed equally to this paper. Correspondence to Elizabeth Conibear: conibear@cmmt.ubc.ca; Stefano Vanni: stefano.vanni@unifr.ch.

https://doi.org/10.1083/jcb.202405042

a membrane-targeting basic patch and hydrophobic β-tongue (Abrami et al., 2021). These structures are required for subsequent acylation of an N-terminal cysteine that confers stable membrane binding and deforms the bilayer, facilitating substrate extraction.

It is not known if these are general principles that apply to other APTs, including the ABHD17 thioesterases. The S-acylated ABHD17 N-terminus is important for localization and activity (Lin and Conibear, 2015; Yokoi et al., 2016), but it remains unclear whether other regions of the protein are important for membrane targeting and substrate extraction. Here, we show that ABHD17A undergoes an activation process involving two distinct structural features. Recruitment of an N-terminal helix followed by acylation is essential for the insertion of a flexible and conserved loop into the bilayer. Membrane binding of the N-terminal helix and loop orients ABHD17A for optimal substrate engagement and activity.

Results

The ABHD17A N-terminus is sufficient for S-acylation and plasma membrane localization

Prior studies showed that deletion of the ABHD17 N-terminus or mutation of all five cysteines in this region blocks S-acylation and plasma membrane targeting (Martin and Cravatt, 2009; Lin and Conibear, 2015; Yokoi et al., 2016). However, the number of modified cysteines remains unknown. To address this question, we focused on ABHD17A, which shows robust activity on NRas (Lin and Conibear, 2015). Using the acyl-PEG exchange (APE) assay, which adds a 5 kD maleimide-functionalized polyethylene glycol (mPEG-maleimide) mass tag to each S-acylation site (Percher et al., 2016), we detected four distinct high molecular weight bands of WT ABHD17A that were absent when the five N-terminal cysteines were mutated to serine (Fig. S1 A). While the fraction of ABHD17A labeled with four mass tags was relatively minor, similar incomplete labeling was observed for endogenous calnexin, a protein known to be dually S-acylated (Percher et al., 2016). This suggests either substoichiometric acylation at steady state, or that the APE reaction was incomplete. Together, these results indicate that at least four, and possibly all five, cysteines in the ABHD17A N-terminus are S-acylated.

It is unclear if other regions of ABHD17 mediate the initial membrane binding that is required for acylation, as reported for APT2 (Abrami et al., 2021). To identify the minimal acylation determinant, we used a sensitive bioluminescence resonance energy transfer (BRET) assay to quantitate its localization at different organelles (Lan et al., 2012). ABHD17A was tagged with the luciferase Rluc8 (donor) and expressed at low levels with different Venus-tagged organelle markers (acceptors). Proximity between the donor and acceptor constructs at organelle membranes results in a high net BRET ratio that reflects the subcellular localization of ABHD17A mutants. We found that replacing all five N-terminal cysteine residues with serine, or deleting the first 19 residues of ABHD17A, significantly decreased plasma membrane localization (Fig. 1 A), consistent with the results of previous immunofluorescence studies (Martin and Cravatt, 2009; Lin and Conibear, 2015). Both mutations also reduced the localization of ABHD17A at the Golgi (Fig. 1 A).

AlphaFold2 (AF2) modeling (Jumper et al., 2021; Varadi et al., 2022) indicates that the N-terminal region of ABHD17A contains an α-helix, with four of the five cysteine residues predicted to lie on or near one face of the helix (Fig. 1, B–D). By labeling cells with the "click-able" palmitate analog 17-octadecynoic acid (17-ODYA), we found that mutation of these four cysteine residues was sufficient to abolish ABHD17A acylation (Fig. 1 E). Moreover, a truncated form of ABHD17A consisting of only its first 17 residues, which includes the 4 cysteines, was acylated as efficiently as a longer fragment that contains all 5 cysteine residues (Fig. 1 F). This minimal N-terminal domain (ABHD17A$^{1–17}$ GFP) was detected at the plasma membrane both by confocal microscopy (Fig. S1, B–E) and by the BRET-based localization assay (Fig. 1 G), and its targeting was abolished by mutating all four cysteine residues to serine. Together, this demonstrates that the region containing the N-terminal helix is necessary and sufficient for ABHD17A acylation and plasma membrane localization and that—in contrast to APT2—regions outside of the acylation motif are not required.

The acylated N-terminus has functions beyond membrane targeting

Reversible S-acylation of APT2 plays an important regulatory role: the acylated, membrane-bound enzyme is stable, but removal of the lipid modification results in ubiquitination and degradation (Abrami et al., 2021). We examined the acylation dynamics of ABHD17A by pulse-chase labeling cells with 17-ODYA in the presence or absence of the deacylase inhibitor hexadecylfluorophosphonate (HDFP; Martin et al., 2011) (Fig. S1, F and G). In contrast to the dynamically acylated protein NRas (Lin and Conibear, 2015) (Fig. S1, H and I), ABHD17A acylation showed little turnover, suggesting a distinct regulatory role.

Our results suggest the minimal N-terminal domain has four acylation sites, yet two membrane anchors are considered sufficient to confer stable membrane association to proteins (Shahinian and Silvius, 1995; Conibear and Davis, 2010). When mutated individually, no single cysteine residue was required for enzyme activity (Fig. S2, A and B). Click labeling did not detect differences in acylation levels of single cysteine mutants (Fig. S2, C and D), whereas significant reductions were observed in most, but not all, double cysteine mutants (Fig. 1, H and I). Some discrepancies could result from incomplete acylation of the overexpressed protein, coupled with differences in the site-specific efficiency of S-acylation or de-acylation events.

Unexpectedly, specific pairwise cysteine substitutions revealed striking differences in enzyme activity despite similar reductions in acylation levels (Fig. 2, A and B). The C14,15S and C10,14S mutations largely abolished deacylation activity on NRas, while C11,15S mutations had minimal impact despite the comparable decrease in acylation. Plasma membrane targeting of these mutants, though reduced, was still observed (Fig. S2 E). Based on these results, we speculated that the dramatic effects on activity could be due to seemingly subtle differences in the position of acyl-modified sites (Fig. S2 F) and that the acylated N-terminus might serve functions beyond membrane targeting.

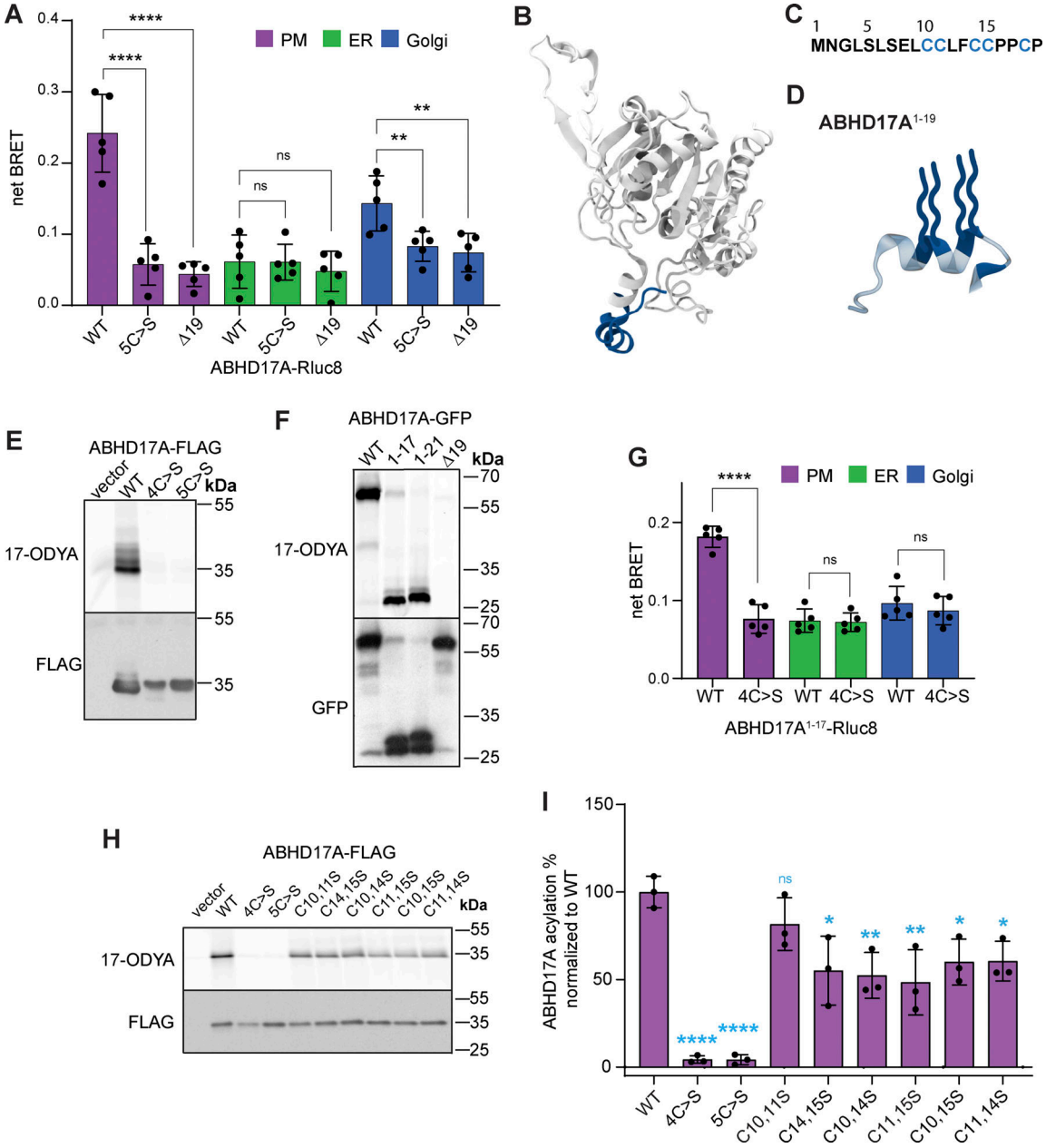

Figure 1. **The N-terminus is necessary and sufficient for S-acylation and plasma membrane localization. (A)** Plasma membrane localization of WT ABHD17A measured with BRET is lost with either mutation of N-terminal cysteine residues or deletion of the N-terminus. Cells were transiently transfected to co-express Rluc8-tagged ABHD17A mutants with a Venus-tagged organelle marker for the plasma membrane, Golgi, or ER. One-way ANOVA with Tukey's multiple comparison test; $n = 5$, ns = $P > 0.05$, ** = $P \leq 0.01$, **** = $P \leq 0.0001$. Error bars depict STDEV. **(B)** AF2-predicted structure of ABHD17A showing the first 19 residues in blue. **(C)** Sequence of the first 19 residues of ABHD17A showing the putative acylated cysteine residues in blue. **(D)** The ABHD17A N-terminus contains a predicted α-helix. Cysteine residues are shown in blue with acyl groups indicated by blue wavy lines attached to Cys10, 11, 14, and 15. **(E)** Acylation of ABHD17A is abolished when either the first four or five N-terminal cysteine residues are mutated to serine as visualized with a click-labeling assay using the palmitate analog 17-ODYA. Upper panel shows 17-ODYA signal and lower panel shows a western blot of total protein detected with FLAG antibody. **(F)** The first 17 residues of ABHD17A (ABHD17A$^{1–17}$) are sufficient for acylation. 17-ODYA signal was detected by click-labeling (upper panel); total protein was detected with GFP antibody (lower panel). **(G)** Plasma membrane localization of the first 17 residues of ABHD17A requires N-terminal cysteine residues. The BRET assay is described in A. One-way ANOVA with Tukey's multiple comparison test; $n = 5$, ns = $P > 0.05$, **** = $P \leq 0.0001$. Error bars indicate STDEV. **(H)** ABHD17A-FLAG acylation in double cysteine mutants. Acylation of ABHD17A-FLAG was detected by click-labeling with 17-ODYA (upper panel). Levels of immunoprecipitated ABHD17A were detected by western blot using anti FLAG antibody (lower panel). **(I)** Quantification ABHD17A-FLAG acylation in H. One-way ANOVA with Tukey's multiple comparison test; $n = 3$, ns = $P > 0.05$, * = $P \leq 0.05$, ** = $P \leq 0.01$, **** = $P \leq 0.0001$. Statistical analysis shows comparison to WT ABHD17A. Error bars indicate STDEV. Source data are available for this figure: SourceData F1.

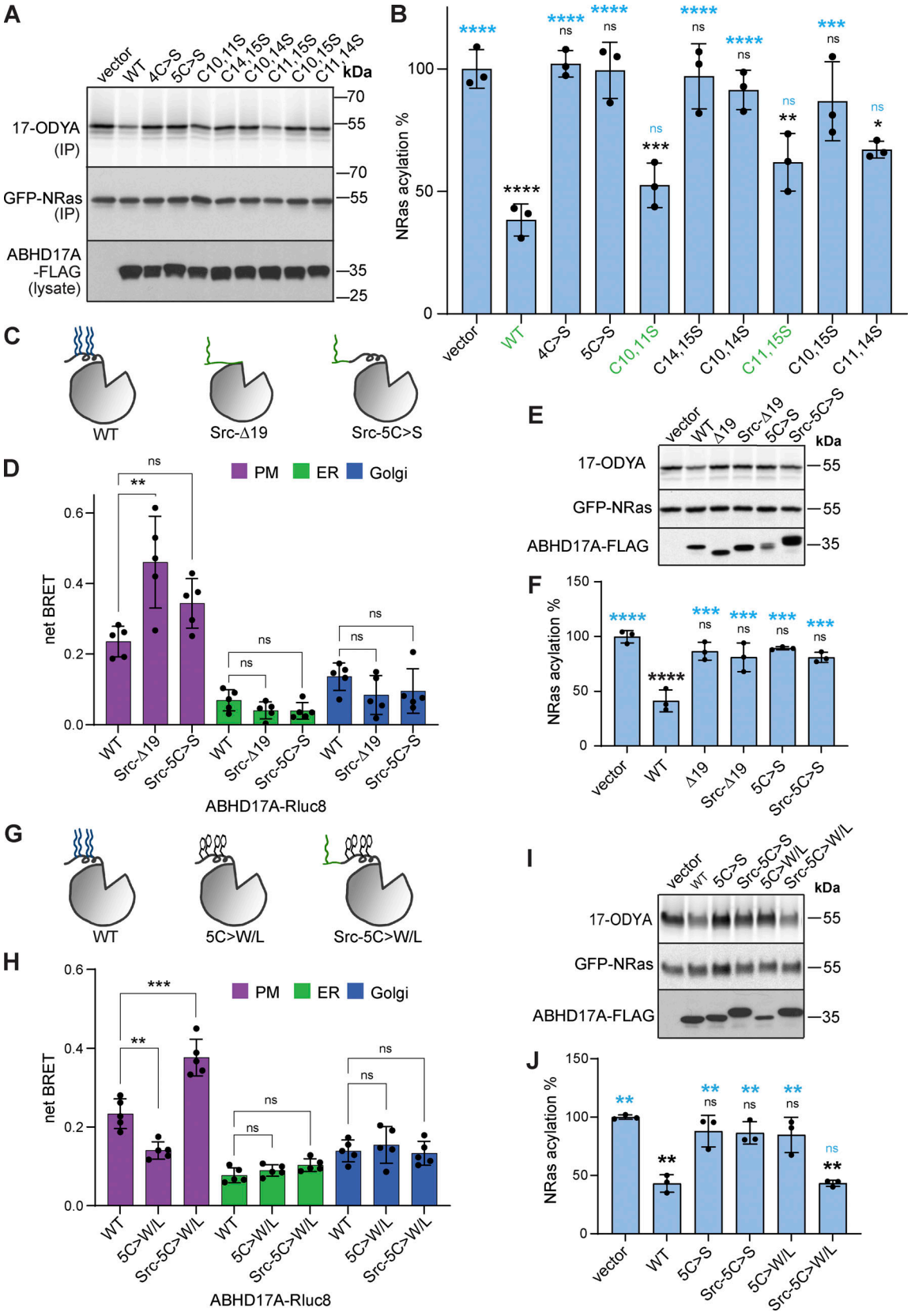

Figure 2. **A targeting-independent role for the ABHD17A N-terminus. (A)** Specific cysteine combinations are required for the activity of FLAG-tagged ABHD17A on NRas. Acylation of GFP-NRas was detected by click-labeling with 17-ODYA (upper panel). Levels of immunoprecipitated NRas (IP; middle panel), or total ABHD17A (lysate; lower panel), were detected by western blot using anti-GFP or FLAG antibody, respectively. **(B)** Quantification of GFP-NRas acylation is shown in A. NRas acylation was normalized to vector. One-way ANOVA with Tukey's multiple comparison test; $n = 3$, ns = $P > 0.05$, * = $P \leq 0.05$, ** = $P \leq 0.01$,

*** = P ≤ 0.001, **** = P ≤ 0.0001. Statistical analysis is depicted with black font (comparison to vector) and blue font (comparison to WT). Error bars indicate STDEV. **(C)** Schematic of ABHD17A constructs. **(D)** The Src myristoylation motif restored plasma membrane localization of ABHD17A lacking either the first 19 residues, or N-terminal cysteine residues, as quantified by BRET analysis. One-way ANOVA with Tukey's multiple comparison test; *n* = 5, ns = P > 0.05, ** = P ≤ 0.01. Error bars indicate STDEV. **(E)** Recruiting non-acylated ABHD17A to the plasma membrane with a Src motif did not restore activity on NRas. Acylation of GFP-NRas was detected by click-labeling with 17-ODYA (upper panel). Levels of immunoprecipitated NRas (middle panel), or total ABHD17A (lower panel), were detected by western blot using anti GFP or FLAG antibody, respectively. **(F)** Quantification of GFP-NRas acylation in E. NRas acylation was normalized to vector. One-way ANOVA with Tukey's multiple comparison test; *n* = 3, ns = P > 0.05, *** = P ≤ 0.001, **** = P ≤ 0.0001. Statistical analysis is depicted with black font (comparison to vector) and blue font (comparison to WT). Error bars indicate STDEV. **(G)** Schematic of ABHD17A constructs with hydrophobic residues in place of N-terminal cysteine residues. **(H)** N-terminal hydrophobic residues localize ABHD17A to the plasma membrane when paired with the Src motif as quantified by BRET analysis. One-way ANOVA with Tukey's multiple comparison test; *n* = 5, ns = P > 0.05, ** = P ≤ 0.01, *** = P ≤ 0.001. Error bars indicate STDEV. **(I)** Pairing the Src motif with hydrophobic N-terminal residues restored activity on GFP-NRas. Acylation of GFP-NRas was detected by click-labeling with 17-ODYA (upper panel). Levels of immunoprecipitated NRas (middle panel), or total ABHD17A (lower panel), were detected by western blot using anti GFP or FLAG antibody, respectively. **(J)** Quantification of NRas acylation in I. NRas acylation was normalized to vector. One-way ANOVA with Tukey's multiple comparison test; *n* = 3, ns = P > 0.05, ** = P ≤ 0.01. Statistical analysis is depicted with black font (comparison to vector) and blue font (comparison to WT). Error bars indicate STDEV. Source data are available for this figure: SourceData F2.

Replacing the acylated N-terminus of ABHD17B with a plasma membrane anchor based on the myristoylated N-terminus of Src did not restore activity on the known substrate PSD-95, highlighting the functional importance of the ABHD17 N-terminus (Yokoi et al., 2016). We hypothesized that this heterologous plasma membrane targeting strategy might circumvent the need for acylation if the N-terminal sequences of ABHD17 were retained. Appending the Src myristoylation motif to either the full-length, acyl-deficient version of ABHD17A (Src-5C>S-ABHD17) or to the N-terminal deletion mutant (Src-Δ19-ABHD17) resulted in efficient plasma membrane targeting in a BRET assay (Fig. 2, C and D). However, neither construct showed significant deacylation activity on NRas (Fig. 2, E and F).

We hypothesized that acyl chains on one face of the helix might help embed it in the bilayer, thereby orienting ABHD17A optimally at the membrane. To test this, we replaced the cysteines with bulky hydrophobic residues (Trp/Leu) and added the Src motif (Src-5C>W/L-ABHD17; Fig. 2 G). This mutant not only localized to the plasma membrane (Fig. 2 H) but also showed significantly restored activity on NRas (Fig. 2, I and J), suggesting that proper membrane embedding of the N-terminal helix is essential for ABHD17A function.

ABHD17A is predicted to interact with membranes through two distinct domains

Our results indicate that the thioesterase activity of ABHD17A depends on a specific interaction between its N-terminal helix ("N-helix") and the lipid bilayer. To understand how ABHD17A interacts with membranes, we turned to molecular dynamics (MD) simulations. First, to assess the quality of the AF2 model of ABHD17A, we analyzed its predicted local distance difference test (pLDDT) score. pLDDT for ABHD17A is very high (>90) for the entire protein, with only two notable exceptions: residues 1–25 (N-terminus) and 42–63 (unstructured loop), which are likely to be flexible in solution (Fig. S3 A). Since the N-terminus is functionally important (Figs. 1 and 2), we next performed all-atom (AA) MD simulations of ABHD17A in solution to investigate its structural and dynamic behavior. Root mean square fluctuation (RMSF) analysis highlights that the N-terminal domain exhibits a significant degree of flexibility along with unstructured linkers (Fig. S3 B). Despite this, the region does not undergo any major conformational changes throughout the simulation (Fig. S3, C and D). Furthermore, the N-terminal domain's sequence includes multiple proline residues (Fig. 1 C), which are well-known for inducing kinks in α-helices. This characteristic explains the presence of an observed helix–turn–helix–coil structure, which remains stable during the entire AA-MD simulation (Fig. S3 C). This structural stability is confirmed by secondary structure timeline analysis and Ramachandran plots (Fig. S3, D and E), which illustrate that the overall fold of the region is maintained over time.

Next, coarse-grained (CG) simulations using the MARTINI force field (Souza et al., 2021) were employed to investigate the interaction between the predicted AF2 model of ABHD17A and a plasma membrane (PM)-like model membrane as this methodology has been shown to accurately predict protein–membrane interfaces for peripheral proteins (Srinivasan et al., 2021; Srinivasan et al., 2024) and has been successfully used to investigate the membrane-binding interface of the thioesterase APT2 (Abrami et al., 2021). We observed that the enzyme primarily interacts with the membrane through two regions: the N-helix and a structurally adjacent loop (residues 222–233, Fig. 3, A and B) that is conserved in all three ABHD17 isoforms and across metazoans (Fig. 3 C). Quantitative analysis of protein–membrane contacts and protein occupancy are shown in Fig. 3, D and E. Of note, analogous simulations started from a structure of ABHD17A with all four cysteines palmitoylated resulted in an identical binding interface with the lipid bilayer (Fig. S4).

To gain deeper insights into ABHD17A's interaction with the PM-like membrane model, we next adopted a finer resolution by means of MD simulations at the atomistic level. To this end, a representative snapshot from the CG simulations was back-mapped to AA and later palmitoylated at four cysteine sites (Fig. 3 F). AA-MD simulations of this configuration show that the CG binding pose remains almost intact, with both the N-terminus (first 21 residues) and the adjacent loop (residues 222–233) penetrating the membrane to an average depth of ~11 and 1 Å, respectively, with respect to the average level of the phosphate groups of the monolayer phospholipids (Fig. 3 G).

Our simulations predict that both N-helix and loop are important for the interaction of ABDH17A with the membrane. To understand the relative contribution of the two regions, we used AA-MD simulations to model different ABHD17A mutants. Upon

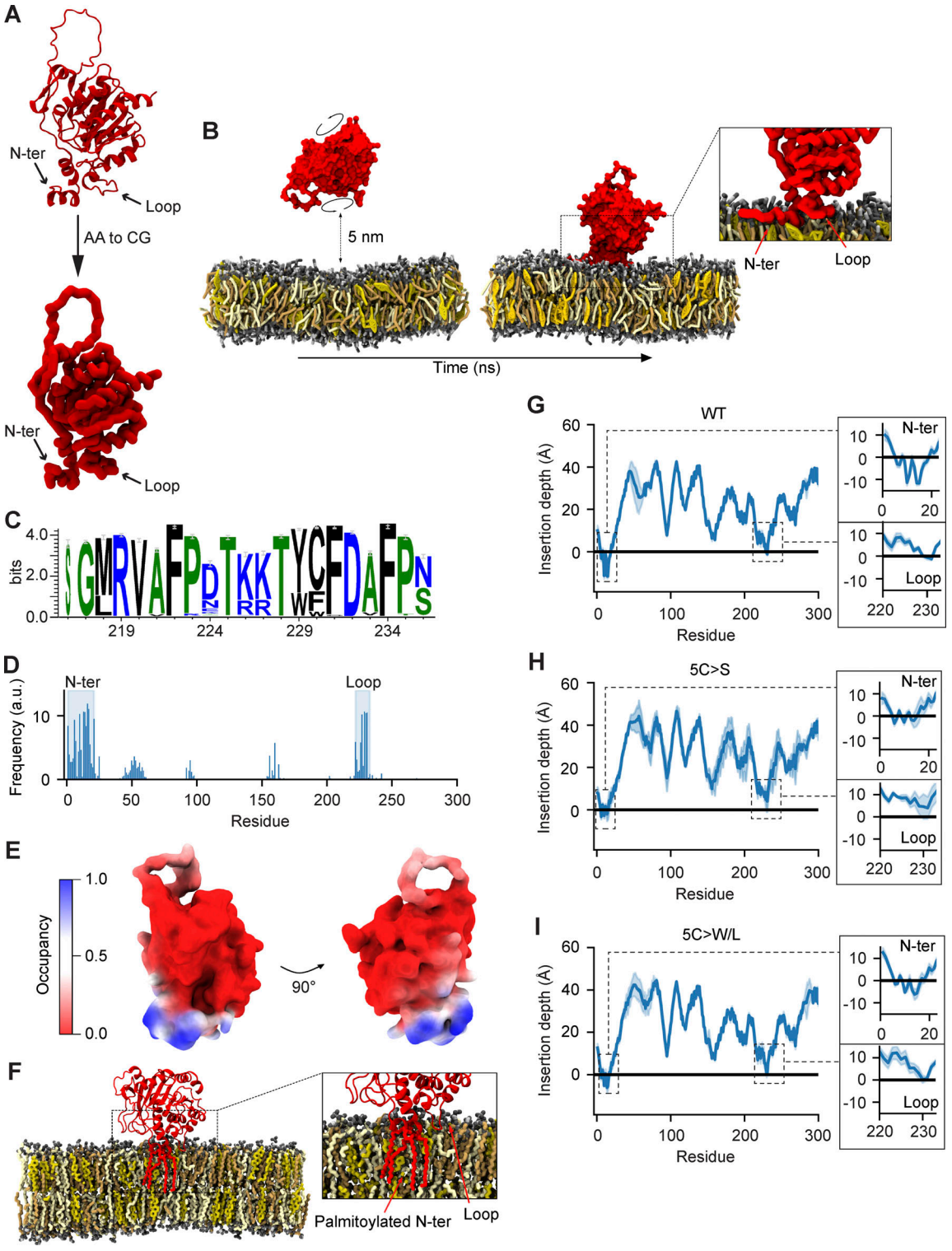

Figure 3. **ABHD17A-membrane interaction is predicted to occur through two distinct domains. (A)** Mapping of full-length AA ABHD17A to CG MARTINI3.0 model. **(B)** Representative mechanism for the binding of ABHD17A (red) to a PM-like membrane (1-palmitoyl-2-oleoylphosphatidylcholine [POPC]: light yellow, 1-palmitoyl-2-oleoylphosphatidylserine [POPS]: orange, cholesterol [CHOL]: yellow) in CG simulations: the protein, initially randomly oriented at a minimum distance of 5 nm from the bilayer, interacts with the membrane via both its N-terminal helix and the adjacent loop. **(C)** Conservation of the loop residues in the three ABHD17 isoforms in metazoans as shown with Weblogo (Crooks et al., 2004). **(D and E)** Membrane interaction of the N-terminal helix and conserved loop shown in the contacts analysis (D) and the occupancy maps (E). **(F)** Snapshot from a representative AA simulation, showing the back-mapped atomistic structure of ABHD17A with the addition of palmitoyl-tails to cysteine residues at its N-terminus. **(G)** Insertion depth analysis of AA simulations confirms that ABHD17A inserts into the membrane via both the palmitoylated N-terminus (residues 1–21) and the adjacent loop (residues 222–233). **(H)** Insertion depth analysis of ABHD17A 5C>S with AA simulations shows mutation of the five N-terminal cysteine residues to serine decreases both N-terminal and loop membrane insertion. **(I)** Restoring N-terminal hydrophobicity of the non-acylated ABHD17A (5C>W/L) rescues insertion depth of the N-terminus and loop in AA simulations. The data shown in G–I are averaged over four replicates, and the error bars indicate STDEV.

mutation of the N-terminal cysteine residues to serine (5C>S), which renders the protein inactive (Fig. 2, A and B), the binding mode of ABHD17 was altered: the insertion depth of the N-terminus decreased significantly (to about 2 Å) and the loop was no longer inserted into the membrane (Fig. 3 H). In agreement with the functional assays (Fig. 2, I and J), mutation of the N-terminal cysteines to bulkier and more hydrophobic residues such as tryptophan (5C>W/L) partially restored the membrane insertion of both the N-helix (to about 5 Å) and loop (to about 0.2 Å; Fig. 3 I). Overall, our data suggest that membrane insertion of the palmitoylated N-helix allows the adjacent loop to insert into the bilayer, and that both interactions contribute to enzyme activity.

Hydrophobic loop residues are important for ABHD17A activity

To test the importance of the conserved loop structure observed in the MD simulations for deacylation activity, we created a series of mutants with four consecutive alanine substitutions spanning the loop (Fig. 4 A). Mutations in the central portion of the loop, which contains polar and charged residues, did not affect enzyme activity on NRas, but mutating outer regions of the loop abolished activity (Fig. 4, B and C). These outer regions contain three conserved hydrophobic residues (F222, Y229, and F231) that lie in a part of the loop that is predicted to insert into the membrane (Fig. 3 B) with protruding side chains that could contribute to membrane binding (Fig. 4 D).

To determine if these hydrophobic loop residues are required for activity, we further made alanine mutations in different combinations (Fig. 4 E). Most of the single and double mutations had relatively minor effects, with F222 and F231 having the greatest effect when mutated together. However, mutating all three hydrophobic residues abolished activity (Fig. 4 F). In AA-MD simulations using the palmitoylated form of ABHD17A, mutation of these hydrophobic loop residues (F/Y>A) resulted in a total loss of membrane insertion for the loop, without affecting the binding of the N-terminus (Fig. 4 G). Taken together, these results suggest that the integrity of both the N-helix and loop are important for membrane binding and activity of ABHD17A.

Mutation of the N-terminal helix and conserved loop alter binding pocket conformation

Many metabolic serine hydrolases have a lid domain that regulates access to the substrate-binding pocket (Devedjiev et al., 2000; Filippova et al., 2013). However, the substrate-binding site of ABHD17, and the mechanisms that regulate substrate binding, are not known. Using a binding pocket prediction algorithm relying on Voronoi tessellation, called FPocket (Le Guilloux et al., 2009), we identified a hydrophobic cavity that represents a potential substrate-binding site (Fig. 5 A). This cavity appears as a cleft in the AF2-predicted structure (Fig. 5 B), with the opening next to the membrane, framed by residues from the N-helix and loop (Fig. 5 C). The catalytic serine is located within the part of the cleft that is distal to the membrane (Fig. 5 D). Based on our top-scoring SwissDock model (Fig. 5, B–D; Grosdidier et al., 2011a), palmitate is predicted to dock in this cleft, with its carboxylate group adjacent to the catalytic serine (Ser190), as would be expected for substrate depalmitoylation. Through AA-MD simulations, we determined that the N-helix and loop regions of ABHD17A are flexible regions that can adopt a wide range of conformations in solution (Fig. S5, A and B), but upon membrane association, they appear to lock into a preferred conformation that could favor substrate insertion into the hydrophobic pocket. Thus, dynamic changes in the positions of the N-helix and/or loop have the potential to control access to the predicted substrate binding site.

Similar to other mSHs, acyl protein thioesterases are irreversibly inhibited by fluorophosphonate (FP) probes, which form a covalent linkage with the active site serine (Creighton, 1993; Piñeiro-Sánchez et al., 1997; Blankman et al., 2007; Martin et al., 2011). To examine the role of the N-helix and loop in regulating substrate binding, we used a competitive activity-based protein profiling (cABPP) assay that measures the ability of a pseudo-substrate FP inhibitor to bind at the active site and prevent subsequent labeling by the fluorescent FP probe TAMRA-FP (Leung et al., 2003; Fig. 5 E). We found that preincubation with the 12-carbon inhibitor isopropyl dodecylfluorophosphonate (IDFP) effectively inhibited TAMRA-FP binding to WT ABHD17A, but not to inactive forms of ABHD17A, such as 5C>S, or the plasma membrane–targeted form of this mutant (Src-5C>S-ABHD17A; Fig. 5, F and G). The altered substrate binding properties of these mutants suggest that changes to either the N-helix or loop that affect their membrane insertion alter the accessibility or conformation of the substrate binding pocket.

We hypothesized that substituting cysteines for bulky hydrophobic residues, which significantly enhanced activity (Fig. 2, I and J), would also restore substrate binding. Indeed, this mutant (Src-5C>W/L-ABHD17A) showed significantly restored IDFP inhibition relative to 5C>S-ABHD17A (Fig. 5, F and G; $P \leq 0.05$), suggesting that the insertion of the N-helix in the bilayer is critical for binding pocket accessibility. Moreover, mutation of all three hydrophobic loop residues (F222, Y229, and F231), which blocked ABHD17A activity, strongly decreased IDFP binding (Fig. 5, H and I). This was not observed when hydrophobic loop residues were mutated individually, supporting the idea that their contribution is partially redundant (Fig. S5, C–F).

Taken together, these results show that mutations that reduce the membrane insertion of either the N-helix or loop alter the conformation of the substrate binding pocket and impair deacylation activity. Conversely, compensatory changes that restore membrane insertion restore pocket conformation and enzyme activity. This supports the model that ABHD17A uses both the N-terminal helix and a conserved loop to bind membranes and orient the hydrophobic pocket in a way that promotes substrate binding.

Discussion

We have shown that the activity of ABHD17A relies on the membrane embedding of two regions that flank the putative substrate binding pocket: the acylated N-terminal helix and a flexible loop. Both elements must be inserted into the membrane to position this binding pocket at the bilayer interface in a way that facilitates substrate entry. While our analysis focused on ABHD17A, all three ABHD17 proteins are predicted to have a

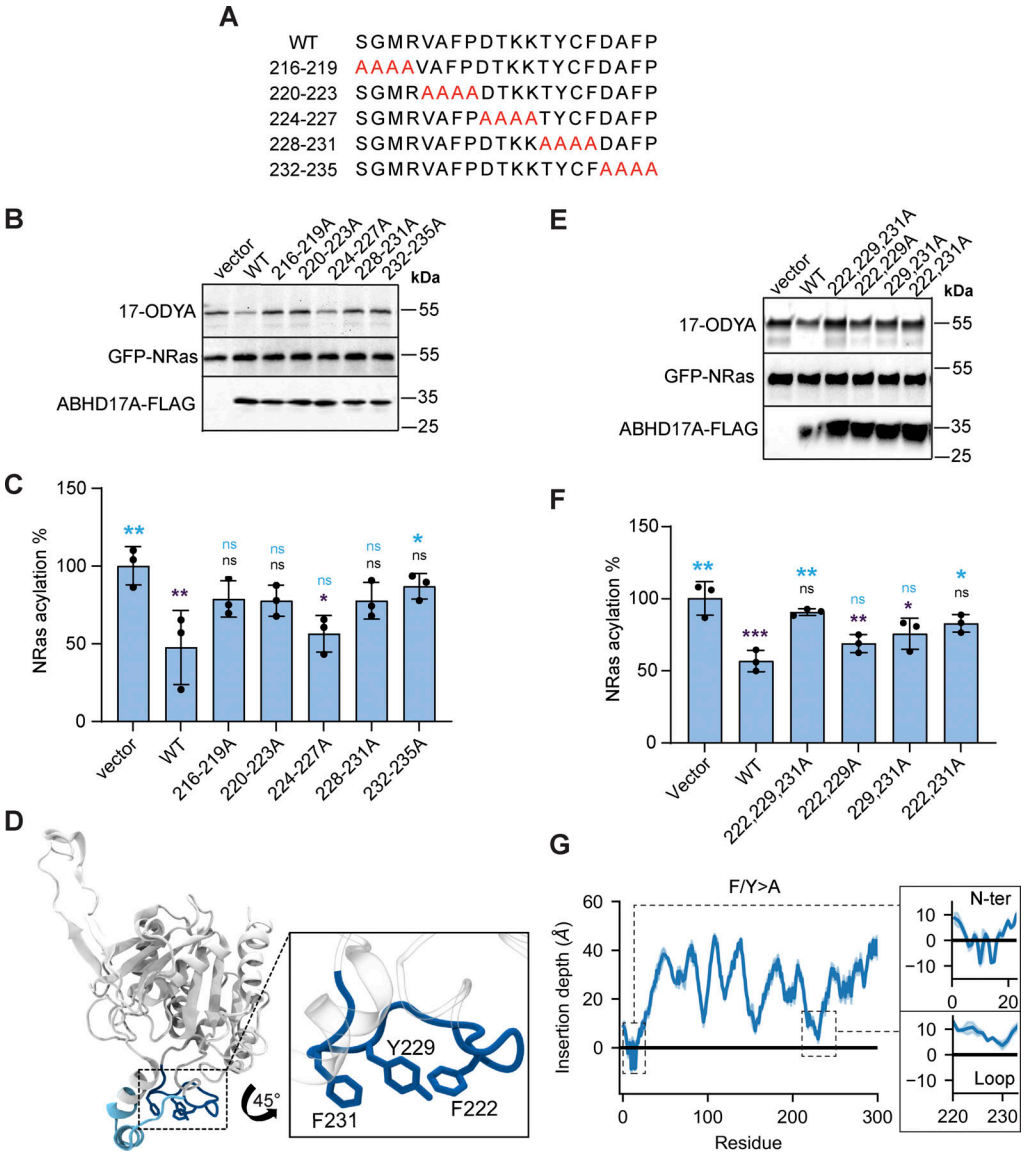

Figure 4. **Hydrophobic loop residues are important for activity. (A)** Schematic of the alanine scan used to determine the regions of the loop required for ABHD17A activity. **(B)** Alanine loop mutants show flanking regions of the loop are important for ABHD17A activity on NRas. Activity of ABHD17A was measured by acylation of GFP-NRas as detected by click-labeling with 17-ODYA (upper panel). Levels of immunoprecipitated NRas (middle panel), or total ABHD17A (lower panel), were detected by western blot using anti-GFP or FLAG antibody, respectively. **(C)** Quantification of GFP-NRas acylation in B. NRas acylation was normalized to vector. One-way ANOVA with Tukey's multiple comparison test; $n = 3$, ns = $P > 0.05$, * = $P \leq 0.05$, ** = $P \leq 0.01$. Statistical analysis is depicted with black font (comparison to vector) and blue font (comparison to WT). Error bars indicate STDEV. **(D)** AF2 predicted structure of ABHD17A showing the loop adjacent to the active site in blue. Inset shows a close-up of the loop and the orientation of the side chains of the three hydrophobic loop residues F222, Y229, and F231. **(E)** Three hydrophobic loop residues (F222, Y229, and F231) are needed for ABHD17A activity on GFP-NRas. Acylation of GFP-NRas was detected by click-labeling with 17-ODYA (upper panel). Levels of immunoprecipitated NRas (middle panel), or total ABHD17A (lower panel), were detected by western blot using anti-GFP or FLAG antibody, respectively. **(F)** Quantification of GFP-NRas acylation in E. NRas acylation was normalized to vector. One-way ANOVA with Tukey's multiple comparison test; $n = 3$, ns = $P > 0.05$, * = $P \leq 0.05$, ** = $P \leq 0.01$, *** = $P \leq 0.001$. Statistical analysis is depicted with black font (comparison to vector) and blue font (comparison to WT). Error bars indicate STDEV. **(G)** Insertion depth analysis shows that mutating hydrophobic loop residues 222, 229, 231 to alanine in AA simulations of acylated ABHD17A impairs membrane insertion of the conserved loop. Source data are available for this figure: SourceData F4.

similar structure that includes an acylated and flexible N-terminus and a conserved loop region, suggesting that they are likely to share the same regulatory mechanism.

Acylation and membrane binding of the N-terminal helix

To be acylated, APTs must first encounter membrane-localized palmitoyltransferases (DHHC-PATs). In the case of APT2, two different regions—a basic patch and a hydrophobic "tongue"—make this initial membrane contact, which leads to the acylation of a single site near the N-terminus (Abrami et al., 2021). In contrast, our work suggests that acylation of the ABHD17 N-terminal domain, which contains a cluster of cysteines on or near a predicted α-helix, does not require other domains. The amphipathic nature of this helix, together with the sulfhydryl

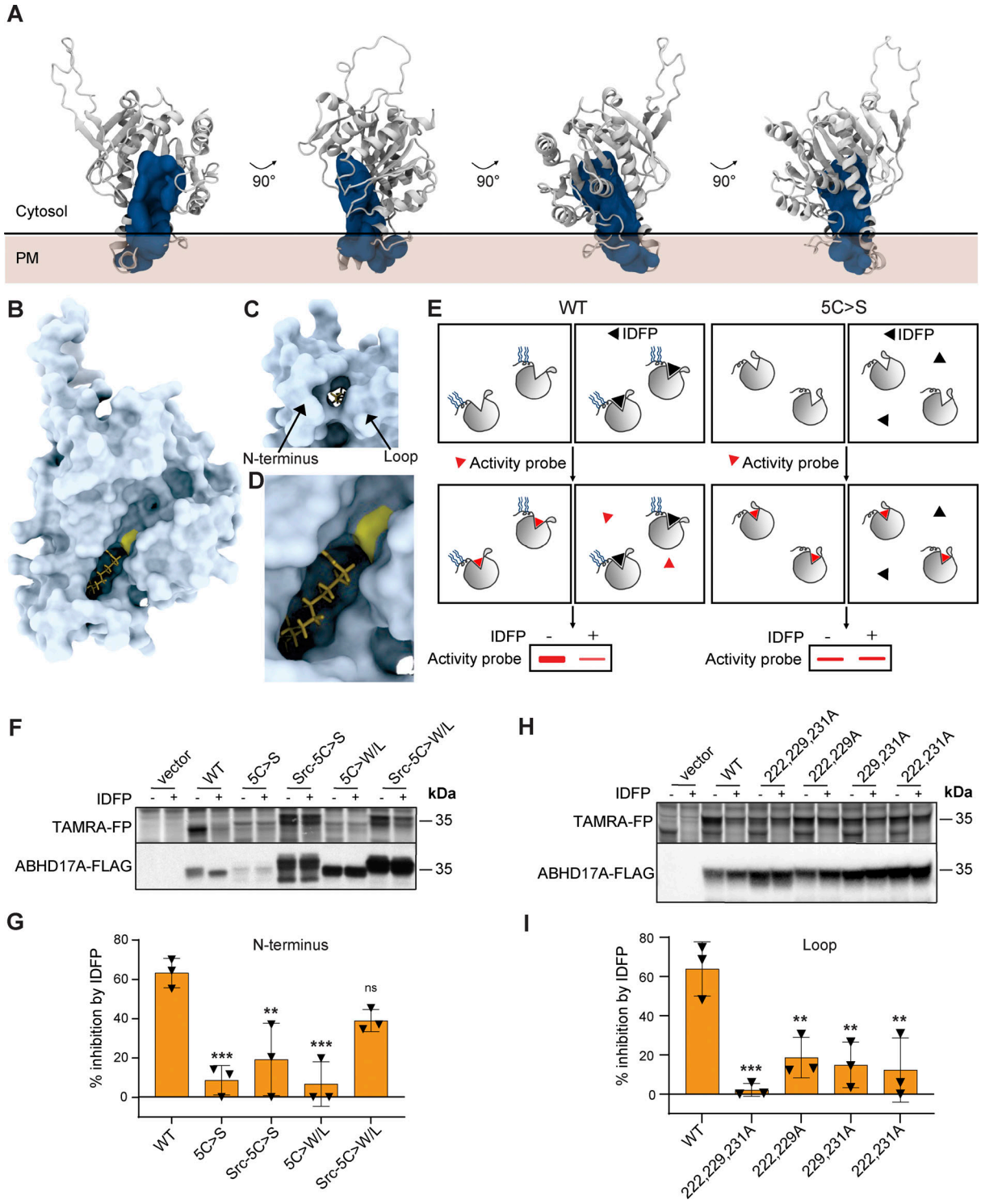

Figure 5. **The N-terminus and loop affect binding pocket conformation. (A)** Pocket analysis identifies one major cavity inside ABHD17A, indicated by the blue solid surface. Its localization close to the membrane interface suggests that the cavity is a potential substrate binding pocket for ABHD17A. **(B–D)** An ABHD17A surface model of the AF2 predicted structure reveals a prominent cleft. Palmitic acid is docked into this cleft by SwissDock (Grosdidier et al., 2011a). The active site serine is shown in yellow. **(C)** Close up of the top-scoring SwissDock model showing palmitic acid interacting with ABHD17A. **(D)** View of the membrane-contacting surface shows the N-terminus and loop are predicted to frame the entrance of the channel. **(E)** Schematic of the cABPP assay used to determine substrate binding of ABHD17A mutants. Cell lysates expressing ABHD17A-FLAG constructs are incubated in the presence or absence of 12-carbon fluorophosphonate inhibitor IDFP in DMSO. Subsequent incubation with the fluorescent activity probe TAMRA-FP covalently labels the catalytic serine of ABHD17A molecules that have not bound the inhibitor. IDFP binding causes a reduction of in-gel fluorescence (left side). Mutations that alter the conformation of the substrate-binding pocket reduce IDFP binding, thus no change in fluorescence is seen (right side). **(F)** The Src myristoylation motif paired with hydrophobic N-terminal residues partially restored the binding pocket conformation of non-acylated ABHD17A mutants. TAMRA-FP binding was visualized with

in-gel fluorescence (upper panel) and total protein was detected by western blot using an anti-FLAG antibody (lower panel). **(G)** Quantification of F depicted by percentage of IDFP inhibition. One-way ANOVA with Tukey's multiple comparison test; $n = 3$, ns = $P > 0.05$, ** = $P \leq 0.01$, *** = $P \leq 0.001$. Statistical analysis shows the comparison to WT ABHD17A. Error bars indicate STDEV. **(H)** Mutation of three hydrophobic loop residues (F222, Y229, and F231) significantly decreased IDFP binding by cABPP analysis. **(I)** Quantification of H depicted by percentage of IDFP inhibition. One-way ANOVA with Tukey's multiple comparison test; $n = 3$, ** = $P \leq 0.01$, *** = $P \leq 0.001$. Statistical analysis shows comparison to WT ABHD17A. Error bars indicate STDEV. Source data are available for this figure: SourceData F5.

side chains of cysteine residues, could favor insertion into the lipid core of the bilayer (Iyer and Mahalakshmi, 2019) and promote the initial membrane interaction needed for ABHD17 to encounter DHHC-PATs.

Because acylation is critical for membrane localization, the dynamic addition and removal of the acyl group was proposed to regulate the activity of APTs by altering access to membrane-localized substrates (Vartak et al., 2014), limiting their concentration by autodeacylation in trans (Kong et al., 2013) or exposing lysine residues that target them for ubiquitination and degradation (Abrami et al., 2021). However, the acylation of ABHD17 on a cluster of four or five cysteines is predicted to shield it from acyl protein thioesterases (Anwar and van der Goot, 2023), which would have to cleave multiple acyl groups to effect membrane release. We did not observe rapid turnover of ABHD17 acylation, thus ABHD17 is unlikely to be regulated by rapid cycling on and off membranes. Instead, our results suggested that acyl chain positioning on the helix was important for activity. Although the reason for this was unclear, the spacing of acylated cysteines could influence helix orientation, subcellular localization, or membrane domain association (Batrouni et al., 2022; El-Husseini et al., 2001).

While the acylated N-terminal helix of ABHD17 is important for membrane targeting, replacing it with a heterologous localization signal compromised activity (Yokoi et al., 2016), suggesting it has another role. We found that full deacylation activity requires the N-terminal helix to associate with the membrane through hydrophobic interactions. In molecular dynamics simulations, the acylated N-terminal helix inserts deeply into the bilayer, which in turn promotes the membrane insertion of the adjacent loop structure. While the insertion of the N-terminal helix is important for loop insertion, the converse is not true: mutations in the loop that block membrane binding and activity do not disrupt the embedding of the N-helix. This suggests that acylation of the N-helix is an initial step that positions ABHD17 for loop insertion and substrate engagement.

The opening of the predicted binding pocket faces the membrane, whereas the catalytic serine is at the base of the pocket, suggesting the lipid substrate must be extracted from the bilayer to enter the binding site. We hypothesize that the membrane insertion of both the N-helix and the loop, which flank this pocket, are important for orienting the enzyme so that the binding pocket is optimally positioned for lipid extraction to occur. Furthermore, the insertion of the acylated N-helix is expected to perturb the bilayer, facilitating this extraction. Indeed, palmitate, the predominant lipid used for S-acylation, decreases membrane fluidity and destabilizes membranes in liposomes (Leekumjorn et al., 2009). Because both tryptophan and phenylalanine insertion also destabilize membranes (Popova et al., 2002), loop binding could also contribute to substrate extraction. Similarly, membrane deformation by APT2 is proposed to facilitate substrate removal and subsequent hydrolysis (Abrami et al., 2021). Thus, acylation may be a common feature of APTs that not only serves as a membrane-targeting signal but also contributes to deacylation activity.

Binding pocket conformation is regulated at the membrane

It is unclear if access to the ABHD17 pocket is dynamically regulated. Many lipases have highly dynamic lid structures that occlude the binding pocket until interaction with a membrane causes the lid to open (Khan et al., 2017). Lid opening and substrate engagement can also cause conformational changes in the binding pocket that promote binding and position the active site residues for cleavage. The APT1/2-like protein FTT258 found in the bacteria *Francisella tularensis* has a flexible loop that acts like a lid to regulate membrane binding, binding pocket accessibility, and enzyme activity (Filippova et al., 2013; Smith et al., 2018). APT1 lacks a lid-like structure but does have a loop that forms part of the binding pocket and undergoes subtle structural rearrangements on substrate binding to accommodate the substrate, which provides isoform selectivity (Won et al., 2016; Harris et al., 2024). APT homologs in plants are also suggested to use sequences adjacent to their active site to select the chain length of substrates (Bürger et al., 2017).

Although ABHD17 lacks an obvious lid structure, we found the integrity of both the N-terminus and loop to be important for the conformation of the binding pocket. In MD simulations, the relative position of the N-helix and loop is highly variable in solution but uniform when bound to membranes. Based on these observations, we favor the hypothesis that the binding and insertion of the N-helix and loop elements into the lipid bilayer stabilizes a conformation that promotes substrate engagement. The location of the active site serine in a deep cleft might help accommodate the acylated peptide as it slides into the active site. Whether ABHD17 proteins undergo additional structural rearrangements in response to substrate binding will be the topic of future studies.

Different organelle membranes have distinct lipid compositions and lipid packing properties that can influence protein binding and insertion (Bigay and Antonny, 2012). It is tempting to speculate that the need for correct insertion of the N-terminal helix and loop regions limits ABHD17 activity to specific organelles or membrane subdomains. This could help explain why ABHD17 appears to act primarily on substrates at the plasma membrane (Remsberg et al., 2021). How ABHD17 localization affects activity and substrate specificity, and whether ABHD17 proteins are also regulated by additional posttranslational modification or expression level (Abazari et al., 2023; Wild et al., 2023)

are important areas of future research. A complete understanding of ABHD17 regulation will be helpful in developing therapeutic approaches that target ABHD17 and will increase our understanding of related thioesterases.

Materials and methods

Plasmids

Venus-tagged KRas-tail, PTP1b-tail, Giantin, and Rluc8-N1 plasmids were gifts from Dr. Nevin Lambert (Augusta University, Augusta, GA, USA; Lan et al., 2012). ABHD17A mutant plasmids (plasmids 5–21 in Table S1) were made with NEBuilder HiFi DNA Assembly (New England Biolabs) using primers (Table S2) to amplify and mutate ABHD17A sequences that were inserted into EcoRI/Bsu36I-digested pABHD17A-FLAG (Lin and Conibear, 2015). The loop mutant plasmids (plasmids 22–33) were made by ligating two PCR products with SacII/BmgBI digested pABHD17A-FLAG. A similar approach was used to create pSrc-Δ19-FLAG, ligating the PCR product into EcoRI/XhoI-digested pABHD17A(Δ19)-FLAG.

To create pABHD17A-EGFP, the EGFP PCR product was ligated into EcoRi/SalI digested pABHD17A-FLAG. NEBuilder HiFi DNA Assembly was used to ligate 1–17 and 1–21 ABHD17A fragments with pABHD17A-EGFP that were digested with EcoRI/AgeI to remove ABHD17 sequences. pABHD17A-Rluc8 constructs were created by PCR amplifying ABHD17A mutants described above. Ligation of the PCR product with EcoRI/BamHI digested pRluc8-N1 was performed with NEBuider HiFi DNA Assembly.

Cell culture and cDNA transfection

COS-7 cells, a non-human primate male cell line from ATCC, were maintained and propagated in high-glucose Dulbecco's Modified Eagle Medium (DMEM; Gibco) supplemented with 10% fetal bovine serum (FBS; Gibco), 4 mM L-glutamine, and 1 mM sodium pyruvate in a humidified incubator at 37°C, 5% CO_2. Cells were checked for mycoplasma contamination every 6 mo by PCR-based analysis. COS-7 cells were grown on 60-mm plates and transfected at 90% confluence using Lipofectamine 2000 (Invitrogen) as per manufacturer's instructions with 1 µg cDNA per plate of each DNA construct for 17-ODYA and cABPP labeling studies. For BRET, cells were grown in 6-well plates and transfected at 90% confluence with 0.5 µg cDNA of acceptor constructs and 0.05 µg cDNA of donor constructs. For fluorescence microscopy, cells were grown on 12-mm glass coverslips (Thermo Fisher Scientific) in 24-well plates and transfected at 90% confluence with 0.4 µg cDNA. Cells were transfected at 90% confluence with 11 µg cDNA for the APE assay.

BRET assays

Cells were washed in PBS, harvested with 0.25% EDTA-Trypsin (Gibco), resuspended in HBSS (Gibco), and transferred to Nunc F96 MicroWell White Polystyrene 96-well plates (Thermo Fisher Scientific). Fluorescence and luminescence measurements were made using a Tecan Spark multimode microplate reader (Tecan). Fluorescence emission was measured at 485 and 530 nm. Coelenterazine h (5 µM; Cayman) was added to cells immediately prior to making measurements. Raw BRET signals were calculated as the emission intensity at 530 nm divided by the emission intensity at 485 nm. Net BRET is the $emission_{acceptor}$/$emission_{donor}$ ratio minus the $emission_{acceptor}$/$emission_{donor}$ ratio measured from cells expressing only the BRET donor.

Acyl-PEG exchange assay

A modified version of the APE assay (Percher et al., 2016; Hurst et al., 2017) was used to assess S-acylation levels. 24 h after transfection, COS-7 cells were washed three times in PBS, frozen at −80°C for 24 h, and lysed in triethanolamine (TEA) buffer (50 mM triethanolamine pH 7.3, 150 mM NaCl) containing 4% SDS, 5 mM EDTA, 5 mM PMSF, and 1X Halt Protease Inhibitor Cocktail (Thermo Fisher Scientific). Clarified lysates were incubated with 25 mM N-ethylmaleimide (NEM; Sigma-Aldrich) for 2 h at RT to block free cysteines. 500 µg of protein in 135 ml TEA buffer was transferred to a new tube and samples were treated with 250 mM 2,3-dimethyl-1,3-butadiene (Sigma-Aldrich) for 1 h at RT with periodic vortexing to remove excess NEM. This was followed by the addition of 1/10th vol of chloroform, 1 min of vortexing, and centrifugation at maximum speed for 5 min. The supernatant was split into two aliquots, with one aliquot receiving 750 mM hydroxylamine treatment for 1 h at RT. A methanol–chloroform extraction was performed, after which the protein precipitates were resuspended in TEA buffer containing 1.33 mM mPEG-maleimide (Sigma-Aldrich), 4 mM EDTA, and 0.2% Triton X-100, and incubated for 2 h at RT. Following methanol–chloroform extraction to remove excess mPEG-maleimide, protein pellets were resuspended in Laemmli buffer (62.5 mM Tris-HCl pH 6.8, 2% SDS, 10% glycerol, 1% 2-mercaptoethanol, and 0.002% Bromophenol blue) and heated at 80°C for 5 min. Samples were analyzed by 10% SDS-PAGE followed by western blotting.

17-ODYA metabolic labeling

20 h following transfection, COS-7 cells were washed once in PBS and starved for 1 h in Base Labelling Media (1 mM L-Glutamine, 1 mM cysteine, and 1 mM sodium pyruvate in cysteine- and methionine-free DMEM). A 30 µM solution of saponified 17-ODYA (Cayman) was prepared by first incubating 6 mM ODYA in 7.2 mM sodium hydroxide at 65°C for 15 min, then adding this to Base Labeling Media containing 20% fatty acid-free BSA. After 2 h in the 17-ODYA solution, cells were washed three times in PBS and placed at −80°C for 24 h. Cells were lysed with TEA lysis buffer (50 mM TEA pH 7.4, 1% TritonX-100, 150 mM NaCl, 2×EDTA-free Halt Protease Inhibitor [Life Technologies]) and vigorously mixed by pipetting. Lysates were cleared by centrifugation at 16,000 × *g* for 15 min at 4°C, and the supernatant protein content was quantified using Bicinchoninic acid (BCA) assay (Life Technologies). 100–130 µg of supernatant was diluted in SDS-sample buffer (200 mM Tris-HCl pH 6.8, 8% SDS, 4% Bromophenol Blue, 40% Glycerol, 1% 2-mercaptoethanol). Samples were heated for 5 min at 95°C and kept at −20°C. The remaining lysate was used for immunoprecipitation and sequential on-bead CuAAC/click chemistry.

For pulse-chase metabolic labeling in the presence of inhibitors, following the 2 h 17-ODYA labeling, cells were washed once in PBS, and chase media (complete DMEM supplemented with 10% FBS and 300 mM palmitic acid) containing 10 µM

HDFP (Cayman) in DMSO was added. At the indicated time points, cells were washed three times in PBS and placed at −80°C for 24 h. Cell lysis was carried out as described above.

Immunoprecipitation and sequential on-bead CuAAC/click chemistry

For immunoprecipitations, Protein A Sepharose beads (GE Healthcare) were washed three times in TEA lysis buffer and preincubated with rabbit anti-GFP antibody for 4 h at 4°C before the addition 500 μg^{-1} mg of transfected COS-7 cell lysates. Immunoprecipitations were carried out for 12–16 h on an end-to-end rotator at 4°C. Sepharose beads were then washed three times in modified radioimmunoprecipitation assay (RIPA) buffer (50 mM TEA pH 7.4, 150 mM NaCl, 1% sodium deoxycholate [wt/vol], 1% TX-100, and 0.1% SDS).

Sequential on-bead click chemistry of immunoprecipitated 17-ODYA–labeled proteins was carried out as previously described (Zhang et al., 2010) with minor modifications. Sepharose beads were washed three times in RIPA buffer and on-bead conjugation of AF647-azide (Invitrogen) to 17-ODYA was carried out for 1 h at RT in 50 µl of freshly mixed click chemistry reaction mixture containing 1 mM TCEP (Aldrich), 1 mM $CuSO_4 \cdot 5H_2O$ (Sigma-Aldrich), 100 µM TBTA (Aldrich), and 100 µM AF647-azide in water. Beads were washed three times with RIPA buffer and resuspended in SDS buffer (200 mM Tris-HCl pH 6.8, 150 mM NaCl, 12% SDS, 50 mM TEA pH 7.4, 4% Bromophenol Blue, 40% glycerol, and 1% 2-mercaptoethanol). Samples were heated for 5 min at 95°C and separated on 10% tris-glycine SDS-PAGE gels for subsequent in-gel fluorescence analyses and then transferred onto nitrocellulose membrane for western blotting. The percent of acylated NRas was calculated using the ratio of ODYA to total purified NRas, normalized to the average value of the vector control.

Lysate samples frozen in SDS-sample buffer were thawed, heated at 95°C for 2 min, sonicated gently, and run on 13% tris-glycine SDS-PAGE gels for western blot analyses.

Competitive activity-base protein profiling

24 h following transfection with ABHD17A constructs, COS-7 cells were washed once in PBS, incubated with 0.25% trypsin for 3 min at 37°C, detached with DMEM + FBS (10%), and collected by centrifugation at 1,000 × *g* for 3 min. The cells were resuspended in 300 µl 50 mM Tris and lysed with gentle sonication on ice. Protein was quantified by BCA assay and 30 µg protein was incubated with IDFP (20 µM; Cayman) in DMSO at RT for 30 min. TAMRA-FP (2 µM final concentration) labeling was carried out at RT for 1 h and quenched with 4× SDS-sample buffer heated to 95°C for 5 min. Samples were separated on SDS–PAGE, analyzed by in-gel fluorescence, and then transferred onto nitrocellulose membrane for western blotting. Inhibition was calculated by dividing the TAMRA-FP signal treated with IDFP by the DMSO control and subtracting this from 100.

In-gel fluorescence analyses

A Typhoon Trio scanner (GE Healthcare) was used to measure the in-gel fluorescence of SDS-PAGE gels. AF647 signals were acquired using the red laser (excitation 633 nm) with a 670BP30 emission filter, and rhodamine signals were acquired with the green laser (excitation 532 nm), with a 580BP30 emission filter. Signals were acquired in the linear range and quantified using Fiji (Schindelin et al., 2012).

Western blotting

Nitrocellulose membranes (50-206-3328; Thermo Fisher Scientific) were blocked in PBST (PBS with 0.1% Tween-20 [Sigma-Aldrich]) containing 3% BSA (Sigma-Aldrich) for 1 h. Membranes were then blotted with corresponding primary antibodies (mouse anti-GFP [11814460001; Roche; RRID:AB_390913] or rabbit anti-FLAG [701629; Thermo Fisher Scientific; RRID: AB_2532497]) in PBST + 3% BSA for 1 h followed by either horseradish peroxidase–conjugated polyclonal goat anti-mouse (115–035-146; Jackson ImmunoResearch Laboratories; RRID: AB_2307392) or horseradish peroxidase–conjugated polyclonal goat anti-rabbit (170-6515; Biorad; RRID: AB_11125142) in PBST + 3% BSA for 1 h. All blots were developed with ECL chemiluminescent reagents (RPN2106; Cytiva) and exposed to Amersham Hyperfilm (CA95-17; VWR). Developed films were scanned, and densitometry was performed in Fiji. The blots in Fig. S1, F and H; and Fig. S2, C and D were imaged on the Fusion FX (Vilber).

Weblogo

ABHD17A homologs were identified at the metazoan level with OrthoDB (Kuznetsov et al., 2023) and aligned with MUSCLE (Edgar, 2004). Weblogo (Crooks et al., 2004) was used to analyze amino acids 216–235 of *Homo sapiens* ABHD17A.

Fluorescence microscopy image acquisition and processing

Coverslips were mounted onto a microscopy slide using ProLong Gold Anti-Fade Mountant (Thermo Fisher Scientific). Microscopy images were acquired at RT on a Leica TCS SP8 Confocal Microscope (Leica Microsystems) with a high-contrast Plan Apochromat 63×/1.30 Glyc CORR CS objective (Leica Microsystems) and an ORCA-Flash4.0 digital camera (Hamamatsu Photonics). Confocal images were acquired with Leica Application Suite X (LASX) 3.5.7 software (Leica Microsystems), followed by deconvolution using Huygens Professional version 23.04 (Scientific Volume Imaging). Representative confocal images were individually adjusted for brightness and contrast using Fiji (Schindelin et al., 2012).

Statistical analysis

GraphPad Prism 10 was used to perform statistical analysis. One-way ANOVA was used to determine the P values of raw data with Tukey's multiple comparison test. P values are reported in figure legends. ns = $P > 0.05$, * = $P \le 0.05$, ** = $P \le 0.01$, *** = $P \le 0.001$, **** = $P \le 0.0001$. Data distribution was assumed to be normal but this was not formally tested.

MD simulations

All MD simulations were carried out starting from the AF2 predicted model of ABHD17A (Uniprot accession number: Q96GS6) and a simple PM-like model membrane constituted of 40%POPC-30%POPS-30%CHOL. CG-MD simulations were carried out using the GROMACS package (version 2021.2) (Abraham

et al., 2015) and employing the MARTINI3 forcefield (Souza et al., 2021). The initial system setup, consisting of ABHD17A positioned ~5 nm above a PM-like membrane, solvated with a 0.15 NaCl solution, was built using the insane.py script (Wassenaar et al., 2015) and subsequently energy-minimized using the steepest descent algorithm. After a 10-ns equilibration conducted in the NPT ensemble, four replicas of 4 µs each were run with a timestep of 20 fs. Using semi-isotropic pressure coupling, the pressure was kept at 1 bar using the Parrinello–Rahman barostat (Parrinello and Rahman, 1981) and applied every 12.0 ps with a compressibility of 3×10^{-4} bar^{-1}. Temperature was maintained constant at 310 K employing the V-rescale thermostat (Bussi et al., 2007). Palmitoylation was modeled using the protocol and parameters from Koukos et al. (2023).

AA-MD simulations were started using a representative snapshot of CG simulations, where ABHD17A was stably anchored to the membrane through both the N-terminus and the structurally adjacent loop. The system was first back-mapped from MARTINI3 CG model to the CHARMM36 AA model (Klauda et al., 2010), employing the CG2AT2 tool (Vickery and Stansfeld, 2021), and later palmitoylated at four sites (CYS10-11-14-15) using CHARMM-GUI tool PDB reader & manipulator (Jo et al., 2008; Jo et al., 2009). Systems containing WT and mutants were equilibrated following the classical CHARMM-GUI 6 step protocol and then simulated using GROMACS software and the CHARMM36m forcefield. Productions were repeated three times for 500 ns each with a timestep of 2 fs in the isothermal–isobaric ensemble (NPT). The Nosé-Hoover thermostat (Evans and Holian, 1985) was used to keep the temperature at 310 K, and the Parrinello–Rahman barostat (Parrinello and Rahman, 1981) was employed, applying a semi-isotropic pressure coupling, to maintain the pressure at 1 bar and a compressibility of 4.5×10^{-5} bar^{-1} every 5 ps. The Particle Mesh Ewald (Darden et al., 1993; Essmann et al., 1995) algorithm was utilized for long-range electrostatic interactions, with a cutoff of 1.2 nm. Lennard–Jones interactions were truncated at 1.2 nm. Bond constraints were treated using linear constraint solver algorithm (Hess et al., 1997).

To investigate the role of the flexibility of the N-terminus and the loop, AA simulations of WT-ABHD17A in solution were performed. The protein was put in a box of water with 0.15 M of NaCl and minimized using the steepest descent algorithm. Six-step CHARMM-GUI equilibration and 1.5 µs NPT production were performed utilizing the same temperature conditions as described before for AA simulations. The pressure was kept at 1 bar through the use of an isotropic barostat (Parrinello and Rahman, 1981) with a compressibility of 4.5×10^{-5} bar^{-1} using $\tau P = 5$ ps.

Protein–membrane contact analysis was conducted on CG systems using ProLint (Sejdiu and Tieleman, 2021), while the occupancy map was generated using GROMACS module *gmx select*. Insertion depth for AA systems was evaluated as in Rogers and Geissler (2023). Cavity pocket detection was performed utilizing the Fpocket software (Le Guilloux et al., 2009), giving as a reference structure for the pocket identification of the AF2 model of ABHD17A. Palmitic acid was docked onto the ABHD17A AF2 model using the SwissDock webserver (https://www.swissdock.ch/) using default parameters (Grosdidier et al., 2011a; Grosdidier et al., 2011b).

To investigate the flexibility of N-terminus and loop regions of ABHD17A WT and mutants in solution versus in membrane, the distance between the center of mass of the two regions was measured using the *gmx pairdist*, and the results were normalized and shown as a probability histogram. All the molecular images were rendered using Visual Molecular Dynamics software (Humphrey et al., 1996). Plots were generated using the python module *matplotlib* (Hunter, 2007).

Online supplemental material

Fig. S1 (complementary to Fig. 1) shows that ABHD17A has at least four acylated cysteine residues that do not show significant turnover and are important for plasma membrane localization. Fig. S2 (complementary to Fig. 1) examines the requirement for specific ABHD17A N-terminal cysteine residues for activity and plasma membrane localization. Fig. S3 shows the dynamic behavior of the ABHD17A N-terminus in AA-MD simulations (complementary to Fig. 3). Fig. S4 shows the effect of palmitoylation on membrane targeting by ABHD17A in CG simulations (complementary to Fig. 3). Fig. S5 shows the effect of mutants on ABHD17A conformation, activity, and binding pocket conformation (complementary to Fig. 5). Table S1 is a list of the plasmids used in this study. Table S2 is a list of the primers used in this study.

Data availability

The data underlying all biochemical experiments are available in the published article and its online supplemental material. MD simulations, all input files, initial configurations, and trajectories saved every 100 ns after water removal, as well as scripts used for analyses can be found at: https://doi.org/10.5281/zenodo.14702866.

Acknowledgments

We thank Dr. Nevin Lambert (Augusta University, Augusta, GA, USA) for the Venus-tagged organelle markers, Rluc8 plasmids (Lan e et al., 2012), and guidance in quantification and statistical analysis of BRET. We also thank Dr. Alexis Shih for helping to develop the IDFP-cABPP assay and thank Dr. Gao Guang and the Life Sciences Institute Imaging Facility at the University of British Columbia for helping with confocal imaging and deconvolution.

This work was supported by funding from the Canada Foundation for Innovation (Leading Edge Fund 30636, to E. Conibear), the Canadian Institutes of Health Research (grant 162184 to E. Conibear), the European Research Council under the European Union's Horizon 2020 Research and Innovation program (grant agreement no. 803952 to S. Vanni), and by grants from the Swiss National Supercomputing Centre under projects ID s1132, s1176, and s1221.

Author contributions: S. Holme: Conceptualization, Data curation, Formal analysis, Investigation, Methodology, Project administration, Resources, Validation, Writing - original draft, J. Sapia: Conceptualization, Data curation, Formal analysis, Investigation, Methodology, Validation, Visualization, Writing - original draft, Writing - review & editing, M. Davey: Investigation,

Methodology, Resources, S. Vanni: Conceptualization, Formal analysis, Funding acquisition, Resources, Supervision, Writing - original draft, Writing - review & editing, E. Conibear: Conceptualization, Data curation, Funding acquisition, Methodology, Project administration, Resources, Supervision, Writing - original draft, Writing - review & editing.

Disclosures: The authors declare no competing interests exist.

Submitted: 14 May 2024
Revised: 7 December 2024
Accepted: 22 January 2025

References

Abazari, D., A.R. Wild, T. Qiu, B.C. Dickinson, and S.X. Bamji. 2023. Activity-dependent post-translational regulation of palmitoylating and depalmitoylating enzymes in the hippocampus. *J. Cell Sci.* 136:jcs260629. https://doi.org/10.1242/jcs.260629

Abraham, M.J., T. Murtola, R. Schulz, S. Páll, J.C. Smith, B. Hess, and E. Lindahl. 2015. GROMACS: High performance molecular simulations through multi-level parallelism from laptops to supercomputers. *SoftwareX*. 1–2:19–25. https://doi.org/10.1016/j.softx.2015.06.001

Abrami, L., M. Audagnotto, S. Ho, M.J. Marcaida, F.S. Mesquita, M.U. Anwar, P.A. Sandoz, G. Fonti, F. Pojer, M. Dal Peraro, and F.G. van der Goot. 2021. Palmitoylated acyl protein thioesterase APT2 deforms membranes to extract substrate acyl chains. *Nat. Chem. Biol.* 17:438–447. https://doi.org/10.1038/s41589-021-00753-2

Anwar, M.U., and F.G. van der Goot. 2023. Refining S-acylation: Structure, regulation, dynamics, and therapeutic implications. *J. Cell Biol.* 222: e202307103. https://doi.org/10.1083/jcb.202307103

Batrouni, A.G., N. Bag, H.T. Phan, B.A. Baird, and J.M. Baskin. 2022. A palmitoylation code controls PI4KIIIα complex formation and PI(4,5)P2 homeostasis at the plasma membrane. *J. Cell Sci.* 135:jcs259365. https://doi.org/10.1242/jcs.259365

Bigay, J., and B. Antonny. 2012. Curvature, lipid packing, and electrostatics of membrane organelles: Defining cellular territories in determining specificity. *Dev. Cell*. 23:886–895. https://doi.org/10.1016/j.devcel.2012.10.009

Blankman, J.L., G.M. Simon, and B.F. Cravatt. 2007. A comprehensive profile of brain enzymes that hydrolyze the endocannabinoid 2-arachidonoylglycerol. *Chem. Biol.* 14:1347–1356. https://doi.org/10.1016/j.chembiol.2007.11.006

Brinster, R.L., J.M. Allen, R.R. Behringer, R.E. Gelinas, and R.D. Palmiter. 1988. Introns increase transcriptional efficiency in transgenic mice. *Proc. Natl. Acad. Sci. USA*. 85:836–840. https://doi.org/10.1073/pnas.85.3.836

Bürger, M., B.C. Willige, and J. Chory. 2017. A hydrophobic anchor mechanism defines a deacetylase family that suppresses host response against YopJ effectors. *Nat. Commun.* 8:2201. https://doi.org/10.1038/s41467-017-02347-w

Bussi, G., D. Donadio, and M. Parrinello. 2007. Canonical sampling through velocity rescaling. *J. Chem. Phys.* 126:014101. https://doi.org/10.1063/1.2408420

Cao, Y., T. Qiu, R.S. Kathayat, S.-A. Azizi, A.K. Thorne, D. Ahn, Y. Fukata, M. Fukata, P.A. Rice, and B.C. Dickinson. 2019. ABHD10 is an S-depalmitoylase affecting redox homeostasis through peroxiredoxin-5. *Nat. Chem. Biol.* 15: 1232–1240. https://doi.org/10.1038/s41589-019-0399-y

Chen, J.J., Y. Fan, and D. Boehning. 2021. Regulation of dynamic protein S-acylation. *Front. Mol. Biosci.* 8:656440. https://doi.org/10.3389/fmolb.2021.656440

Conibear, E., and N.G. Davis. 2010. Palmitoylation and depalmitoylation dynamics at a glance. *J. Cell Sci.* 123:4007–4010. https://doi.org/10.1242/jcs.059287

Creighton, T.E. 1993. *Proteins: Structures and Molecular Properties*. MacMillan, New York, NY, USA.

Crooks, G.E., G. Hon, J.-M. Chandonia, and S.E. Brenner. 2004. WebLogo: A sequence logo generator. *Genome Res.* 14:1188–1190. https://doi.org/10.1101/gr.849004

Darden, T., D. York, and L. Pedersen. 1993. Particle mesh Ewald: An N·log(N) method for Ewald sums in large systems. *J. Chem. Phys.* 98:10089–10092. https://doi.org/10.1063/1.464397

Devedjiev, Y., Z. Dauter, S.R. Kuznetsov, T.L.Z. Jones, and Z.S. Derewenda. 2000. Crystal structure of the human acyl protein thioesterase I from a single X-ray data set to 1.5 A. *Structure*. 8:1137–1146. https://doi.org/10.1016/S0969-2126(00)00529-3

Dixon, C.L., N.R. Martin, M.J. Niphakis, B.F. Cravatt, and G.D. Fairn. 2023. Attenuating ABHD17 enhances S-palmitoylation, membrane localization and signal transduction of NOD2 and Crohn's disease-associated variants. *bioRxiv*. https://doi.org/10.1101/2023.12.20.572362 (Preprint posted December 21, 2023).

Edgar, R.C. 2004. MUSCLE: Multiple sequence alignment with high accuracy and high throughput. *Nucleic Acids Res.* 32:1792–1797. https://doi.org/10.1093/nar/gkh340

El-Husseini, A.-D., S.E. Craven, S.C. Brock, and D.S. Bredt. 2001. Polarized targeting of peripheral membrane proteins in neurons. *J. Biol. Chem.* 276:44984–44992. https://doi.org/10.1074/jbc.M103049200

Essmann, U., L. Perera, M.L. Berkowitz, T. Darden, H. Lee, and L.G. Pedersen. 1995. A smooth particle mesh Ewald method. *J. Chem. Phys.* 103:8577–8593. https://doi.org/10.1063/1.470117

Evans, D.J., and B.L. Holian. 1985. The Nose–Hoover thermostat. *J. Chem. Phys.* 83:4069–4074. https://doi.org/10.1063/1.449071

Filippova, E.V., L.A. Weston, M.L. Kuhn, B. Geissler, A.M. Gehring, N. Armoush, C.T. Adkins, G. Minasov, I. Dubrovska, L. Shuvalova, et al. 2013. Large scale structural rearrangement of a serine hydrolase from Francisella tularensis facilitates catalysis. *J. Biol. Chem.* 288:10522–10535. https://doi.org/10.1074/jbc.m112.446625

Greaves, J., and L.H. Chamberlain. 2010. S-acylation by the DHHC protein family. *Biochem. Soc. Trans.* 38:522–524. https://doi.org/10.1042/BST0380522

Grosdidier, A., V. Zoete, and O. Michielin. 2011a. SwissDock, a protein-small molecule docking web service based on EADock DSS. *Nucleic Acids Res.* 39:W270–W277. https://doi.org/10.1093/nar/gkr366

Grosdidier, A., V. Zoete, and O. Michielin. 2011b. Fast docking using the CHARMM force field with EADock DSS. *J. Comput. Chem.* 32:2149–2159. https://doi.org/10.1002/jcc.21797

Harris, W.T. III, I. Altieri, I. Gieck, and R.J. Johnson. 2024. A conserved but structurally divergent loop in acyl protein thioesterase 1 regulates its catalytic activity, ligand binding, and folded stability. *Proteins*. 92: 693–704. https://doi.org/10.1002/prot.26661

Hess, B., H. Bekker, H.J.C. Berendsen, and J.G.E.M. Fraaije. 1997. LINCS: A linear constraint solver for molecular simulations. *J. Comput. Chem.* 18: 1463–1472. https://doi.org/10.1002/(SICI)1096-987X(199709)18:12<1463::AID-JCC4>3.0.CO;2-H

Humphrey, W., A. Dalke, and K. Schulten. 1996. VMD: Visual molecular dynamics. *J. Mol. Graph.* 14:33–38, 27–28. https://doi.org/10.1016/0263-7855(96)00018-5

Hunter, J.D. 2007. Matplotlib: A 2D graphics environment. *Comput. Sci. Eng.* 9: 90–95. https://doi.org/10.1109/MCSE.2007.55

Hurst, C.H., D. Turnbull, F. Plain, W. Fuller, and P.A. Hemsley. 2017. Maleimide scavenging enhances determination of protein S-palmitoylation state in acyl-exchange methods. *Biotechniques*. 62:69–75. https://doi.org/10.2144/000114516

Iyer, B.R., and R. Mahalakshmi. 2019. Hydrophobic characteristic is energetically preferred for cysteine in a model membrane protein. *Biophys. J.* 117:25–35. https://doi.org/10.1016/j.bpj.2019.05.024

Jo, S., T. Kim, V.G. Iyer, and W. Im. 2008. CHARMM-GUI: A web-based graphical user interface for CHARMM. *J. Comput. Chem.* 29:1859–1865. https://doi.org/10.1002/jcc.20945

Jo, S., J.B. Lim, J.B. Klauda, and W. Im. 2009. CHARMM-GUI Membrane Builder for mixed bilayers and its application to yeast membranes. *Biophys. J.* 97:50–58. https://doi.org/10.1016/j.bpj.2009.04.013

Jumper, J., R. Evans, A. Pritzel, T. Green, M. Figurnov, O. Ronneberger, K. Tunyasuvunakool, R. Bates, A. Žídek, A. Potapenko, et al. 2021. Highly accurate protein structure prediction with AlphaFold. *Nature*. 596: 583–589. https://doi.org/10.1038/s41586-021-03819-2

Kathayat, R.S., P.D. Elvira, and B.C. Dickinson. 2017. A fluorescent probe for cysteine depalmitoylation reveals dynamic APT signaling. *Nat. Chem. Biol.* 13:150–152. https://doi.org/10.1038/nchembio.2262

Khan, F.I., D. Lan, R. Durrani, W. Huan, Z. Zhao, and Y. Wang. 2017. The lid domain in lipases: Structural and functional determinant of enzymatic properties. *Front. Bioeng. Biotechnol.* 5:16. https://doi.org/10.3389/fbioe.2017.00016

Klauda, J.B., R.M. Venable, J.A. Freites, J.W. O'Connor, D.J. Tobias, C. Mondragon-Ramirez, I. Vorobyov, A.D. MacKerell Jr., and R.W. Pastor. 2010. Update of the CHARMM all-atom additive force field for lipids: Validation on six lipid types. *J. Phys. Chem. B*. 114:7830–7843. https://doi.org/10.1021/jp101759q

Kong, E., S. Peng, G. Chandra, C. Sarkar, Z. Zhang, M.B. Bagh, and A.B. Mukherjee. 2013. Dynamic palmitoylation links cytosol-membrane shuttling of acyl-protein thioesterase-1 and acyl-protein thioesterase-2 with that of proto-oncogene H-ras product and growth-associated protein-43. *J. Biol. Chem.* 288:9112–9125. https://doi.org/10.1074/jbc.M112.421073

Koukos, P.I., S. Dehghani-Ghahnaviyeh, C. Velez-Vega, J. Manchester, D.P. Tieleman, J.S. Duca, P.C.T. Souza, and Z. Cournia. 2023. Martini 3 force field parameters for protein lipidation post-translational modifications. *J. Chem. Theory Comput.* 19:8901–8918. https://doi.org/10.1021/acs.jctc.3c00604

Kuznetsov, D., F. Tegenfeldt, M. Manni, M. Seppey, M. Berkeley, E.V. Kriventseva, and E.M. Zdobnov. 2023. OrthoDB v11: Annotation of orthologs in the widest sampling of organismal diversity. *Nucleic Acids Res.* 51: D445–D451. https://doi.org/10.1093/nar/gkac998

Lan, T.-H., Q. Liu, C. Li, G. Wu, and N.A. Lambert. 2012. Sensitive and high resolution localization and tracking of membrane proteins in live cells with BRET. *Traffic*. 13:1450–1456. https://doi.org/10.1111/j.1600-0854.2012.01401.x

Le Guilloux, V., P. Schmidtke, and P. Tuffery. 2009. Fpocket: An open source platform for ligand pocket detection. *BMC Bioinformatics*. 10:168. https://doi.org/10.1186/1471-2105-10-168

Leekumjorn, S., H.J. Cho, Y. Wu, N.T. Wright, A.K. Sum, and C. Chan. 2009. The role of fatty acid unsaturation in minimizing biophysical changes on the structure and local effects of bilayer membranes. *Biochim. Biophys. Acta*. 1788:1508–1516. https://doi.org/10.1016/j.bbamem.2009.04.002

Leung, D., C. Hardouin, D.L. Boger, and B.F. Cravatt. 2003. Discovering potent and selective reversible inhibitors of enzymes in complex proteomes. *Nat. Biotechnol.* 21:687–691. https://doi.org/10.1038/nbt826

Lin, H. 2021. Protein cysteine palmitoylation in immunity and inflammation. *FEBS J.* 288:7043–7059. https://doi.org/10.1111/febs.15728

Lin, D.T.S., and E. Conibear. 2015. ABHD17 proteins are novel protein depalmitoylases that regulate N-Ras palmitate turnover and subcellular localization. *Elife*. 4:e11306. https://doi.org/10.7554/eLife.11306

Main, A., and W. Fuller. 2022. Protein S-palmitoylation: Advances and challenges in studying a therapeutically important lipid modification. *FEBS J.* 289:861–882. https://doi.org/10.1111/febs.15781

Martin, B.R., and B.F. Cravatt. 2009. Large-scale profiling of protein palmitoylation in mammalian cells. *Nat. Methods*. 6:135–138. https://doi.org/10.1038/nmeth.1293

Martin, B.R., C. Wang, A. Adibekian, S.E. Tully, and B.F. Cravatt. 2011. Global profiling of dynamic protein palmitoylation. *Nat. Methods*. 9:84–89. https://doi.org/10.1038/nmeth.1769

McClafferty, H., H. Runciman, and M.J. Shipston. 2020. Site-specific deacylation by ABHD17a controls BK channel splice variant activity. *J. Biol. Chem.* 295:16487–16496. https://doi.org/10.1074/jbc.RA120.015349

Mesquita, F.S., L. Abrami, M.E. Linder, S.X. Bamji, B.C. Dickinson, and F.G. van der Goot. 2024. Mechanisms and functions of protein S-acylation. *Nat. Rev. Mol. Cell Biol.* 25:488–509. https://doi.org/10.1038/s41580-024-00700-8

Muszbek, L., G. Haramura, J.E. Cluette-Brown, E.M. Van Cott, and M. Laposata. 1999. The pool of fatty acids covalently bound to platelet proteins by thioester linkages can be altered by exogenously supplied fatty acids. *Lipids*. 34:S331–S337. https://doi.org/10.1007/BF02562334

Parrinello, M., and A. Rahman. 1981. Polymorphic transitions in single crystals: A new molecular dynamics method. *J. Appl. Phys.* 52:7182–7190. https://doi.org/10.1063/1.328693

Percher, A., S. Ramakrishnan, E. Thinon, X. Yuan, J.S. Yount, and H.C. Hang. 2016. Mass-tag labeling reveals site-specific and endogenous levels of protein S-fatty acylation. *Proc. Natl. Acad. Sci. USA*. 113:4302–4307. https://doi.org/10.1073/pnas.1602244113

Piñeiro-Sánchez, M.L., L.A. Goldstein, J. Dodt, L. Howard, Y. Yeh, H. Tran, W.S. Argraves, and W.T. Chen. 1997. Identification of the 170-kDa melanoma membrane-bound gelatinase (seprase) as a serine integral membrane protease. *J. Biol. Chem.* 272:7595–7601. https://doi.org/10.1074/jbc.272.12.7595

Popova, A.V., A.G. Heyer, and D.K. Hincha. 2002. Differential destabilization of membranes by tryptophan and phenylalanine during freezing: The roles of lipid composition and membrane fusion. *Biochim. Biophys. Acta*. 1561:109–118. https://doi.org/10.1016/S0005-2736(01)00462-X

Ramzan, F., F. Abrar, G.G. Mishra, L.M.Q. Liao, and D.D.O. Martin. 2023. Lost in traffic: Consequences of altered palmitoylation in neurodegeneration. *Front. Physiol.* 14:1166125. https://doi.org/10.3389/fphys.2023.1166125

Remsberg, J.R., R.M. Suciu, N.A. Zambetti, T.W. Hanigan, A.J. Firestone, A. Inguva, A. Long, N. Ngo, K.M. Lum, C.L. Henry, et al. 2021. ABHD17 regulation of plasma membrane palmitoylation and N-Ras-dependent cancer growth. *Nat. Chem. Biol.* 17:856–864. https://doi.org/10.1038/s41589-021-00785-8

Rogers, J.R., and P.L. Geissler. 2023. Ceramide-1-phosphate transfer protein enhances lipid transport by disrupting hydrophobic lipid-membrane contacts. *PLoS Comput. Biol.* 19:e1010992. https://doi.org/10.1371/journal.pcbi.1010992

Rosier, K., M.T. McDevitt, J. Smet, B.J. Floyd, M. Verschoore, M.J. Marcaida, C.A. Bingman, I. Lemmens, M. Dal Peraro, J. Tavernier, et al. 2021. Prolyl endopeptidase-like is a (thio)esterase involved in mitochondrial respiratory chain function. *iScience*. 24:103460. https://doi.org/10.1016/j.isci.2021.103460

Savinainen, J.R., J.Z. Patel, T. Parkkari, D. Navia-Paldanius, J.J.T. Marjamaa, T. Laitinen, T. Nevalainen, and J.T. Laitinen. 2014. Biochemical and pharmacological characterization of the human lymphocyte antigen B-associated transcript 5 (BAT5/ABHD16A). *PLoS One*. 9:e109869. https://doi.org/10.1371/journal.pone.0109869

Schindelin, J., I. Arganda-Carreras, E. Frise, V. Kaynig, M. Longair, T. Pietzsch, S. Preibisch, C. Rueden, S. Saalfeld, B. Schmid, et al. 2012. Fiji: An open-source platform for biological-image analysis. *Nat. Methods*. 9: 676–682. https://doi.org/10.1038/nmeth.2019

Sejdiu, B.I., and D.P. Tieleman. 2021. ProLint: A web-based framework for the automated data analysis and visualization of lipid-protein interactions. *Nucleic Acids Res.* 49:W544–W550. https://doi.org/10.1093/nar/gkab409

Shahinian, S., and J.R. Silvius. 1995. Doubly-lipid-modified protein sequence motifs exhibit long-lived anchorage to lipid bilayer membranes. *Biochemistry*. 34:3813–3822. https://doi.org/10.1021/bi00011a039

Smith, M.A., W.K. Phillips, P.L. Rabin, and R.J. Johnson. 2018. A dynamic loop provides dual control over the catalytic and membrane binding activity of a bacterial serine hydrolase. *Biochim. Biophys. Acta Proteins Proteom.* 1866:925–932. https://doi.org/10.1016/j.bbapap.2018.05.012

Souza, P.C.T., R. Alessandri, J. Barnoud, S. Thallmair, I. Faustino, F. Grünewald, I. Patmanidis, H. Abdizadeh, B.M.H. Bruininks, T.A. Wassenaar, et al. 2021. Martini 3: A general purpose force field for coarse-grained molecular dynamics. *Nat. Methods*. 18:382–388. https://doi.org/10.1038/s41592-021-01098-3

Srinivasan, S., V. Zoni, and S. Vanni. 2021. Estimating the accuracy of the MARTINI model towards the investigation of peripheral protein-membrane interactions. *Faraday Discuss.* 232:131–148. https://doi.org/10.1039/D0FD00058B

Srinivasan, S., A. Di Luca, D. Álvarez, A.T. John Peter, C. Gehin, M.A. Lone, T. Hornemann, G. D'Angelo, and S. Vanni. 2024. The conformational plasticity of structurally unrelated lipid transport proteins correlates with their mode of action. *PLoS Biol.* 22:e3002737. https://doi.org/10.1371/journal.pbio.3002737

Tortosa, E., Y. Adolfs, M. Fukata, R.J. Pasterkamp, L.C. Kapitein, and C.C. Hoogenraad. 2017. Dynamic palmitoylation targets MAP6 to the axon to promote microtubule stabilization during neuronal polarization. *Neuron*. 94:809–825.e7. https://doi.org/10.1016/j.neuron.2017.04.042

Ulengin-Talkish, I., M.A.H. Parson, M.L. Jenkins, J. Roy, A.Z.L. Shih, N. St-Denis, G. Gulyas, T. Balla, A.-C. Gingras, P. Várnai, et al. 2021. Palmitoylation targets the calcineurin phosphatase to the phosphatidylinositol 4-kinase complex at the plasma membrane. *Nat. Commun.* 12: 6064. https://doi.org/10.1038/s41467-021-26326-4

Varadi, M., S. Anyango, M. Deshpande, S. Nair, C. Natassia, G. Yordanova, D. Yuan, O. Stroe, G. Wood, A. Laydon, et al. 2022. AlphaFold protein structure database: Massively expanding the structural coverage of protein-sequence space with high-accuracy models. *Nucleic Acids Res.* 50:D439–D444. https://doi.org/10.1093/nar/gkab1061

Vartak, N., B. Papke, H.E. Grecco, L. Rossmannek, H. Waldmann, C. Hedberg, and P.I.H. Bastiaens. 2014. The autodepalmitoylating activity of APT maintains the spatial organization of palmitoylated membrane proteins. *Biophys. J.* 106:93–105. https://doi.org/10.1016/j.bpj.2013.11.024

Vickery, O.N., and P.J. Stansfeld. 2021. CG2AT2: An enhanced fragment-based approach for serial multi-scale molecular dynamics simulations. *J. Chem. Theory Comput.* 17:6472–6482. https://doi.org/10.1021/acs.jctc.1c00295

Wassenaar, T.A., H.I. Ingólfsson, R.A. Böckmann, D.P. Tieleman, and S.J. Marrink. 2015. Computational lipidomics with insane: A versatile tool for generating custom membranes for molecular simulations. *J. Chem. Theory Comput.* 11:2144–2155. https://doi.org/10.1021/acs.jctc.5b00209

Wild, A.R., P.W. Hogg, S. Flibotte, S. Kochhar, R.B. Hollman, K. Haas, and S.X. Bamji. 2023. CellPalmSeq: A curated RNAseq database of palmitoylating and de-palmitoylating enzyme expression in human cell types and

laboratory cell lines. *Front. Physiol.* 14:1110550. https://doi.org/10.3389/fphys.2023.1110550

Won, S.J., D. Davda, K.J. Labby, S.Y. Hwang, R. Pricer, J.D. Majmudar, K.A. Armacost, L.A. Rodriguez, C.L. Rodriguez, F.S. Chong, et al. 2016. Molecular mechanism for isoform-selective inhibition of acyl protein thioesterases 1 and 2 (APT1 and APT2). *ACS Chem. Biol.* 11:3374–3382. https://doi.org/10.1021/acschembio.6b00720

Won, S.J., M. Cheung See Kit, and B.R. Martin. 2018. Protein depalmitoylases. *Crit. Rev. Biochem. Mol. Biol.* 53:83–98. https://doi.org/10.1080/10409238.2017.1409191

Xu, J., C. Hedberg, F.J. Dekker, Q. Li, K.M. Haigis, E. Hwang, H. Waldmann, and K. Shannon. 2012. Inhibiting the palmitoylation/depalmitoylation cycle selectively reduces the growth of hematopoietic cells expressing oncogenic Nras. *Blood.* 119:1032–1035. https://doi.org/10.1182/blood-2011-06-358960

Xu, J., W. Gu, K. Ji, Z. Xu, H. Zhu, and W. Zheng. 2018. Sequence analysis and structure prediction of ABHD16A and the roles of the ABHD family members in human disease. *Open Biol.* 8:180017. https://doi.org/10.1098/rsob.180017

Yokoi, N., Y. Fukata, A. Sekiya, T. Murakami, K. Kobayashi, and M. Fukata. 2016. Identification of PSD-95 depalmitoylating enzymes. *J. Neurosci.* 36:6431–6444. https://doi.org/10.1523/JNEUROSCI.0419-16.2016

Zhang, M.M., L.K. Tsou, G. Charron, A.S. Raghavan, and H.C. Hang. 2010. Tandem fluorescence imaging of dynamic S-acylation and protein turnover. *Proc. Natl. Acad. Sci. USA.* 107:8627–8632. https://doi.org/10.1073/pnas.0912306107

Zheng, S., X. Que, S. Wang, Q. Zhou, X. Xing, L. Chen, C. Hou, J. Ma, P. An, Y. Peng, et al. 2023. ZDHHC5-mediated NLRP3 palmitoylation promotes NLRP3-NEK7 interaction and inflammasome activation. *Mol. Cell.* 83:4570–4585.e7. https://doi.org/10.1016/j.molcel.2023.11.015

Zhou, B., Q. Hao, Y. Liang, and E. Kong. 2023. Protein palmitoylation in cancer: Molecular functions and therapeutic potential. *Mol. Oncol.* 17:3–26. https://doi.org/10.1002/1878-0261.13308

Supplemental material

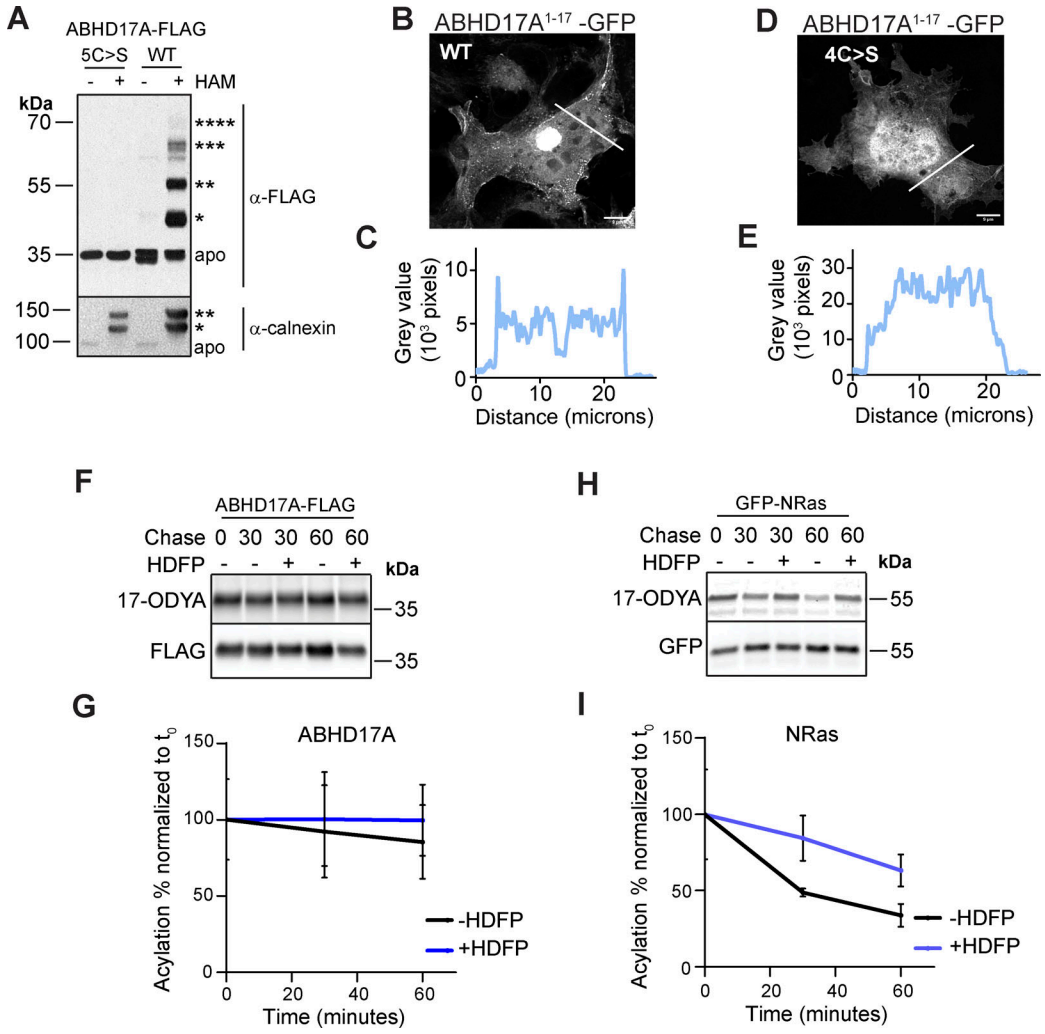

Figure S1. **ABHD17A has at least four stable acylation sites that are required for plasma membrane localization. (A)** An APE assay detects at least four S-acylation sites in ABHD17A. The addition of a mass tag causes a size shift that is proportional to the number of acyl modifications; the number of acylation sites is denoted by asterisks. The doubly acylated calnexin serves as a control. **(B and C)** The first 17 residues of ABHD17A localize to the plasma membrane. The white line through the cell was used for the line scan in C. **(D and E)** The plasma membrane localization of the first 17 residues of ABHD17A is lost when cysteine residues are mutated to serine. A line scan (E) depicts the higher signal intensity in the cytosol of the cell when the N-terminal cysteine residues are mutated to serine of ABHD17A. **(B and D)** show representative confocal images of fixed cells, with the intensity increased to show the plasma membrane localization of WT compared to the cytosolic signal of 4C>S. **(F)** ABHD17A acylation does not show significant turnover as measured by 17-ODYA labeling followed by a chase in the presence or absence of 10 µM HDFP. **(G)** Quantification of ABHD17A acylation in F. Error bars indicate standard deviation (STDEV). **(H)** NRas acylation does show significant turnover when measured with click-labeling followed by a chase in the presence or absence of 10 µM HDFP, as described in F. **(I)** Quantification of NRas acylation in H. Source data are available for this figure: SourceData FS1.

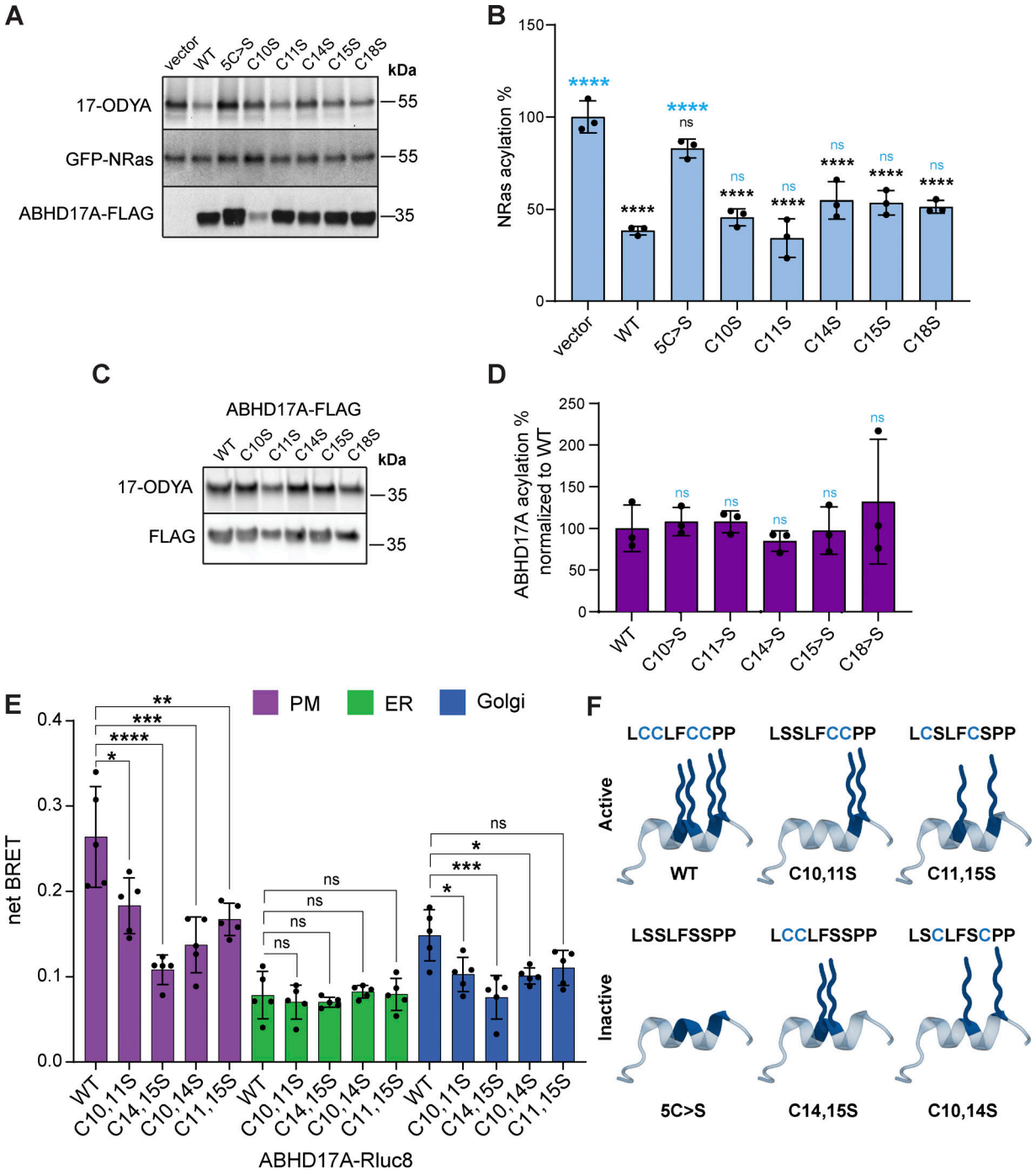

Figure S2. **Specific cysteine residues are required for activity and plasma membrane localization. (A)** Activity of ABHD17A is not affected by individual mutation of N-terminal cysteine residues to serine. Acylation of GFP-NRas was detected by click-labeling with 17-ODYA (upper panel). Levels of immunoprecipitated NRas (middle panel) or total ABHD17A (lower panel) were detected by western blot using anti-GFP or FLAG antibody, respectively. **(B)** Quantification of GFP-NRas acylation in A. NRas acylation was normalized to vector. One-way ANOVA with Tukey's multiple comparison test; $n = 3$, ns = $P > 0.05$, **** = $P \leq 0.0001$. Statistical analysis is depicted with black font (comparison to vector) and blue font (comparison to WT). Error bars indicate STDEV. **(C)** Acylation of ABHD17A was not affected by mutating N-terminal cysteine residues individually. Acylation of ABHD17A-FLAG was detected by click-labeling with 17-ODYA (upper panel). Levels of immunoprecipitated ABHD17A were detected by western blot using anti FLAG antibody (lower panel). **(D)** Quantification ABHD17A-FLAG acylation in C. One-way ANOVA with Tukey's multiple comparison test; $n = 3$, ns = $P > 0.05$. Statistical analysis shows comparison to WT ABHD17A. Error bars indicate STDEV. **(E)** Representative double cysteine mutant constructs show decreased plasma membrane association in BRET analysis. One-way ANOVA with Tukey's multiple comparison test; $n = 5$, ns = $P > 0.05$, * = $P \leq 0.05$, ** = $P \leq 0.01$, *** = $P \leq 0.001$, **** = $P \leq 0.0001$. Error bars indicate STDEV. **(F)** Schematic of the predicted N-terminal helix of ABHD17A cysteine mutants showing acylation patterns of active and inactive constructs. Acyl groups are depicted with blue wavy lines. Source data are available for this figure: SourceData FS2.

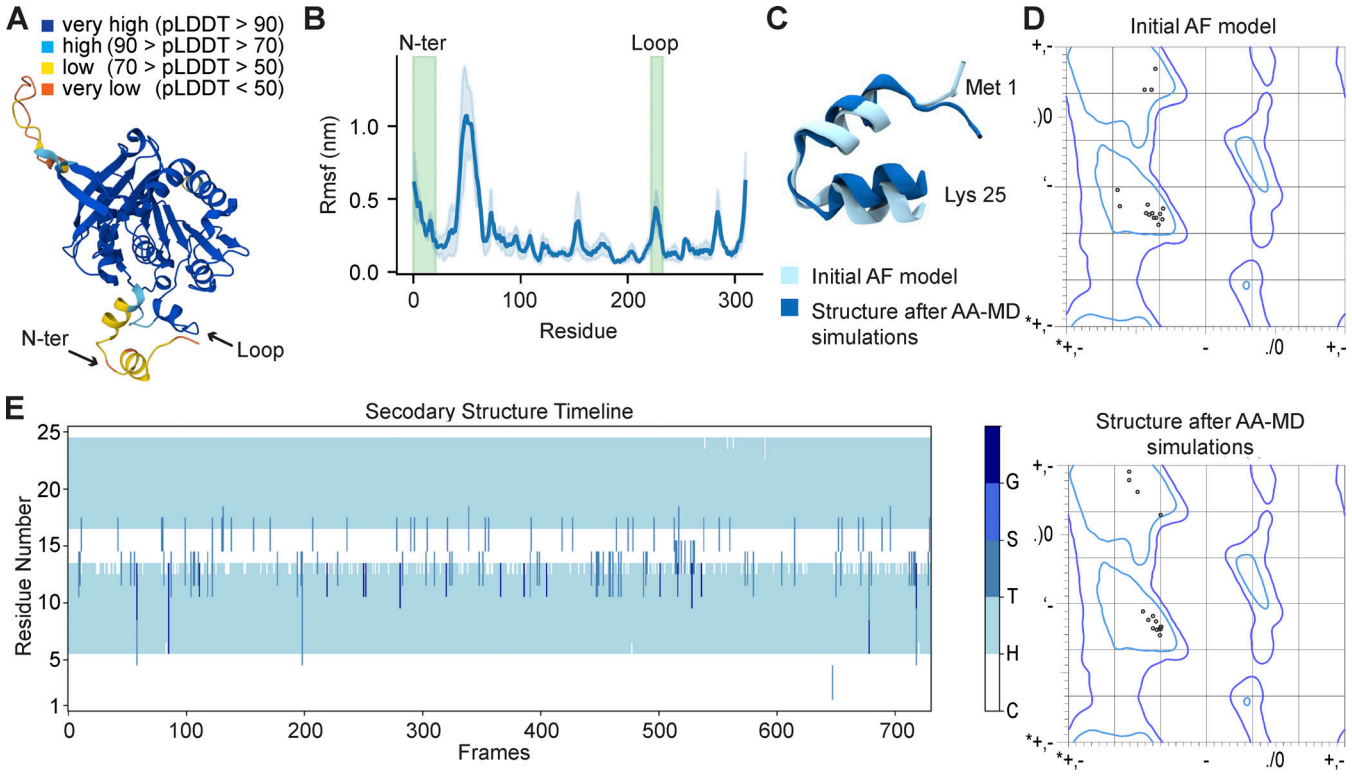

Figure S3. **Dynamic behavior of ABHD17A N-terminus in AA-MD simulations in solution. (A)** AF model of ABHD17A with coloring based on pLDDT score. **(B)** RMSF analysis indicates that the N-terminal helix and the conserved loop (green boxes) are flexible regions. **(C)** Superimposition of N-terminal domain (residue 1–25) of the AF predicted model before and after AA-MD simulations in solution. **(D)** Ramachandran plots of ABHD17A N-terminal domain (resid 1–25) before and after AA-MD simulations, highlighting the good stereochemical quality of the model. **(E)** Secondary structure conservation of the N-terminal domain (resid 1–25) along the MD simulation: the analysis was conducted on a representative replica taken from AA-MD simulations of ABHD17A full-length in solution (legend: G = 3–10 helix, S = Sheet, T = Turn, H = Helix, C = Coil).

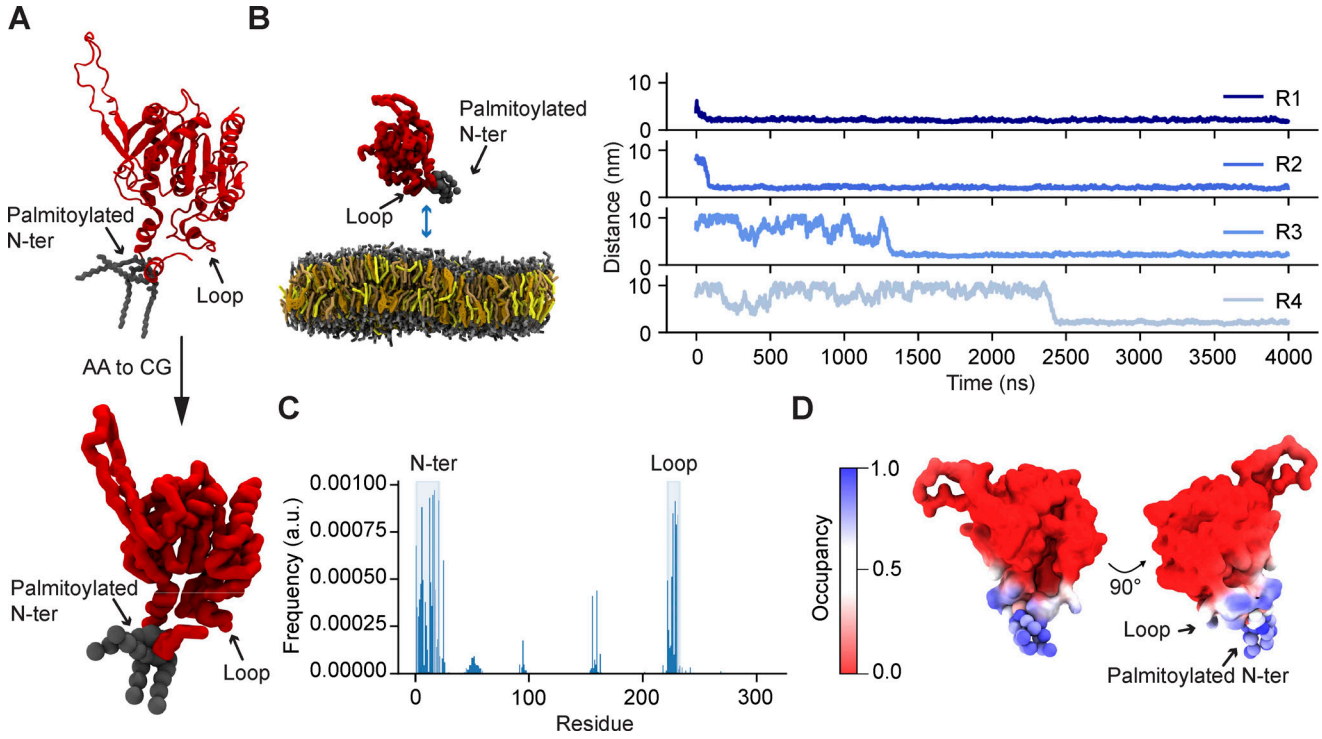

Figure S4. **Effect of palmitoylation on membrane targeting by ABHD17A in CG simulations. (A)** Mapping of palmitoylated AA ABHD17A full length to CG MARTINI3.0 model, with four palmitoyl chains at its N-terminus. **(B)** Minimum distance analysis of CG-MD simulations of palmitoylated ABHD17A. In all four independent replicas, the protein shows association with the nearby membrane, on a μs timescale. **(C and D)** Membrane interaction of the palmitoylated N-terminal helix and conserved loop shown in the contacts analysis (C) and the occupancy maps (D).

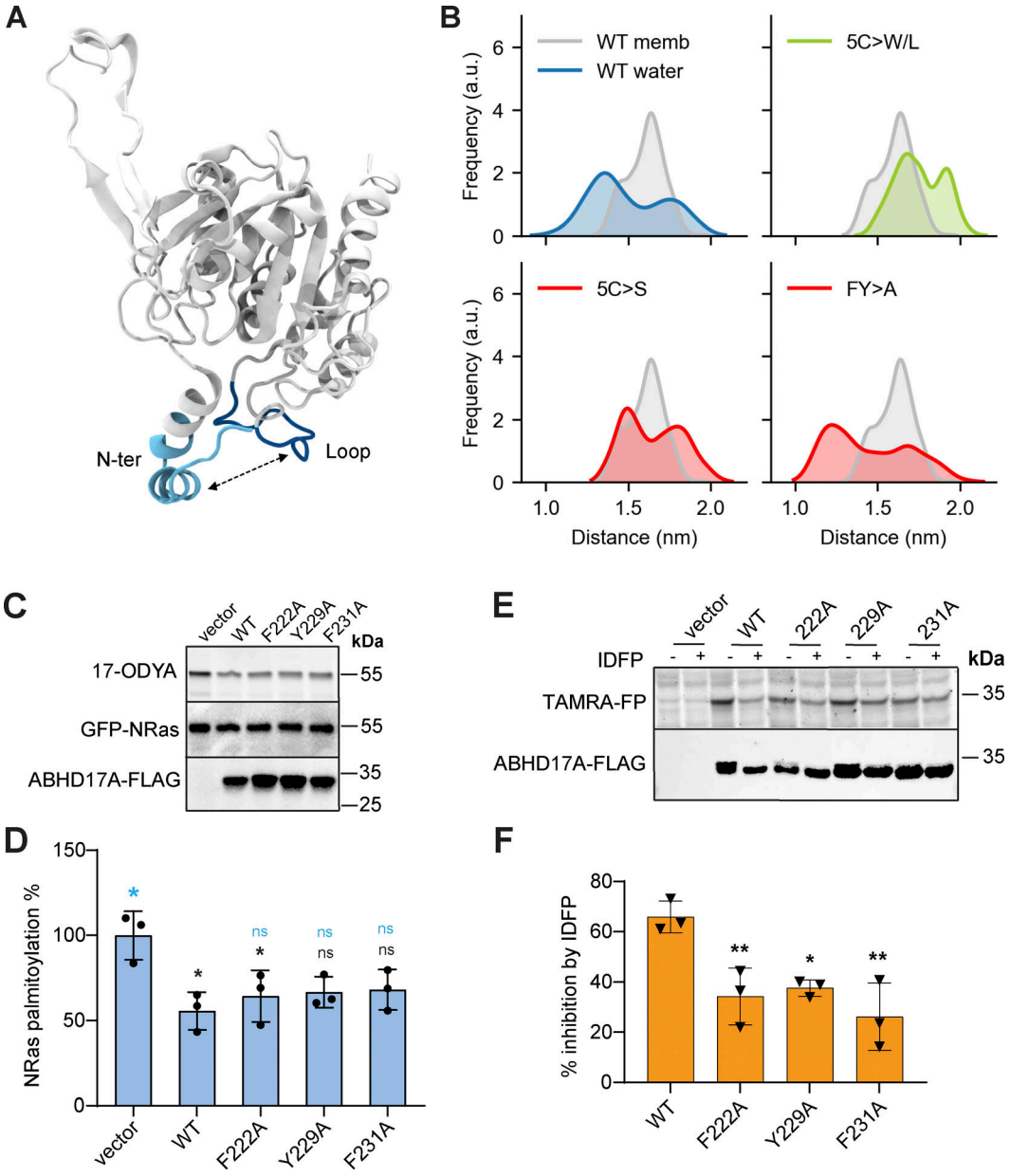

Figure S5. **Effect of mutations in N-terminus or loop on ABHD17A conformation. (A)** The N-terminus and nearby loop, which are responsible for the binding of ABHD17A to the membrane, are localized at the entrance of the hypothesized substrate binding pocket. **(B)** The probability distributions of the distance between the N-terminus and loop from AA simulations, in water versus bound to the membrane (upper left), indicate that the opening of the cavity displays conformational flexibility, which could influence substrate entry/exit. When the N-terminal cysteine residues are mutated to serine (lower left) or the hydrophobic loop residues are mutated to alanine (lower right), the N-terminus and loop regions are more dynamic, likely due to decreased membrane binding. When the hydrophobicity of the N-terminus is restored in the 5C>W/L mutant (upper left), the enzyme displays a smaller range of conformations, which may be optimal for substrate binding. Histograms were smoothed using the kernel density estimation method. **(C)** Individual mutation of hydrophobic loop residues to alanine has little effect on ABHD17A activity. GFP-NRas acylation was detected by 17-ODYA click-labeling. Levels of immunoprecipitated NRas (middle panel), or total ABHD17A (lower panel), were detected by western blot using anti GFP or FLAG antibody, respectively. **(D)** Quantification of NRas acylation in C. Acylation was normalized to vector. One-way ANOVA with Tukey's multiple comparison test; $n = 3$, ns = $P > 0.05$, * = $P \leq 0.05$. Statistical analysis is depicted with black font (comparison to vector) and blue font (comparison to WT). Error bars indicate STDEV. **(E)** Individual mutation of the hydrophobic loop residues to alanine has a small effect on substrate binding in cABPP analysis. **(F)** Quantification of E depicted by percentage of IDFP inhibition. One-way ANOVA with Tukey's multiple comparison test; $n = 3$, * = $P \leq 0.05$, ** = $P \leq 0.01$. Statistical analysis shows comparison to WT ABHD17A. Error bars indicate STDEV. Source data are available for this figure: SourceData FS5.

Provided online are Table S1 and Table S2. Table S1 lists the plasmids used in this study. Table S2 lists the primers used in this study.